POLITECNICO DI MILANO
Scuola di Ingegneria Industriale

Master of Science in
Space Engineering

DESIGN OF AN EXPERIMENTAL DEVICE FOR THE CHARACTERIZATION OF SOLAR CELLS IN LILT ENVIRONMENTS

Relatore: **Prof. Franco Bernelli**
Correlatore: **Ing. Francesco Topputo**

Thesis by:

Gioele ZGRAGGEN
Matr. n. 754829

Academic Year 2012-2013

"The best way to learn to fly
a spacecraft is to fly one."
Wild Andy

Ringraziamenti

Vorrei innanzitutto ringraziare l'Ing. Francesco Topputo, per avermi dato la disponibilità di lavorare a questa tesi, ma soprattutto per avermi seguito in ogni momento, grazie ad i suoi insegnamenti ho imparato molto durante l'arco di questa tesi. Diverse persone sono state fondamentali per il lavoro svolto e senza di esse non sarei riuscito a svolgere tutto il lavoro: l'Ing. Giuseppe D'Amore, grazie alle sue conoscenze in elettrotecnica mi ha aiutato nella realizzazione della scheda elettronica, così come l'Ing. Alberto Dolara, l'Ing. Mauro Massari, grazie alle sue conoscenze ed alla sua disponibilità sono riuscito a risolvere diversi problemi, l'Ing. Silvio Ferragina e l'Ing. Mauro Strada per la realizzazione della serpentina di raffreddamento, l'Ing. Maria Rosaria Pagano, l'Ing. Paolo Rubini e l'Ing. Alessandro Mattironi per i consigli e gli aiuti nelle varie prove in laboratorio, infine il mio vicino di tesi Andrea Binci.

Oltre a loro voglio ringraziare tutta la mia famiglia e i miei amici che mi son sempre stati vicini in tutti questi anni.

Abstract

On March 2, 2004 at 07:17 UT the Rosetta Mission left from Kourou on the Ariane 5 G+ launcher with the aim to arrive in 2014 on the comet 67P/Churyumov-Gerasimenko. After reaching the comet, Rosetta will release its lander Philae that will land on the comet. Its nominal life is guaranteed by non-rechargeable primary batteries for a period of five comet days; further extension of the mission may be provided by six solar panels on the faces of the lander Philae.

The first purpose of this thesis is to create an environment similar to that of the comet, mainly consisting in low temperatures (around -100°C) and low solar intensity (0.11 Solar Constant); such conditions allows us study the behaviour of the solar cells in both beginning and end of life (BOL, EOL). Indeed, for the EOL case, such test has never been performed before. For this reason it has been built an experimental apparatus so as to be able to perform the tests in these conditions and to store all the data into a computing environment.

Keywords:

Solar cells; Low Intensity Low Temperature; Characterization I-V curve; Experimental device; Philae; Rosetta mission.

Sommario

Il 2 Marzo 2004 alle 07:17 UT è partita da Kourou con il lanciatore Ariane 5 G+ la missione Rosetta con lo scopo di arrivare nel 2014 sulla cometa 67P/Churyumov-Gerasimenko. Dopo aver raggiunto la cometa, Rosetta sgancerà il suo lander Philae che atterrerà sulla cometa. La durata nominale di questa fase è di 5 giorni ed è garantita da batterie primarie non ricaricabili, un' ulteriore prolungamento della missione può essere reso possibile da sei pannelli fotovoltaici presenti sulla facce di Philae.
Lo scopo di questa tesi è di ricreare un ambiente simile a quello della cometa, ossia a basse temperature (attorno ai -100°C) e bassa intensità solare (0.11 Solar Constant). Tali condizioni sono infatti necessarie per studiare il comportamento delle celle solari a inizio vita (BOL) e fine vita (EOL), dato che per il secondo caso non sono mai stati effettuati dei test. Per questo motivo si è costruito un apparato sperimentale in modo tale da poter effettuare delle prove in tali condizioni e elaborare tutti i dati direttamente al calcolatore.

Parole chiave:
Celle solari; Bassa intensità bassa temperatura; Caratterizzazione curva I-V; Apparato sperimentale; Philae; Missione Rosetta.

Contents

List of Figures

List of Tables

Estratto in italiano

Progettazione di un apparato sperimentale per la caratterizzazione di celle solari in ambiente LILT

In queste pagine vengono ripresi i principali temi che sono trattati all'interno della tesi, lo scopo di essa era andare a costruire un apparato sperimentale in grado di caratterizzare le celle solari del lander Philae.

L'effetto fotovoltaico Il principio di funzionamento delle celle solari è la conversione fotovoltaica, che converte l'energia della luce direttamente in energia elettrica.
Le celle solari sono essenzialmente costituite da strati di materiale semiconduttore con caratteristiche diverse. I principali materiali semiconduttori di interesse per questo tipo di applicazione sono solidi cristallini, costituiti da elementi della IV colonna della tavola periodica di Mendelejev (silicio e germanio), o composti binari costituiti da elementi della III e V colonna (ad esempio arseniuro di gallio, GaAs). L'effetto fotovoltaico è la creazione di tensione o di corrente elettrica in un materiale per esposizione alla luce. Quando la luce del sole o di qualsiasi altra luce è incidente su di una superficie di materiale, gli elettroni presenti nella banda di valenza di un atomo metallico assorbono l'energia e, essendo eccitato, saltano alla banda di conduzione e diventano liberi. Ora questi elettroni liberi sono attratti da un elettrodo caricato positivamente e quindi il circuito si completa e l'energia della luce viene convertita in energia elettrica.

La missione rosetta È una missione dell'agnzia spaziale europea ESA, sviluppata a partire dagli anni '90 con l'obbiettivo di atterrare e campionare il nucleo di una cometa. Rosetta è stata lanciata nel 2004 con lo scopo di raggiungere la cometa 67P/Churyumov-Gerasimenko nel 2014 ad una distanza di 3 AU, dopo aver viaggiato dieci anni nello spazio e sorvolato gli asteroidi

2867 Steins e Lutetia 21.
Una volta raggiunta la cometa l'orbiter Rosetta inizierà ad orbitare intorno ad essa, in modo da identificare il miglior posto e traiettoria per farci atterrare il suo lander Philae, esso sarà poi responsabile di effettuare una serie di campionamenti sulla superficie.
Durante i dieci anni di volo l'orbiter, grazie a due pannelli solari lunghi 14 metri, si occuperà di alimentare il lander, ma dal momento dello sgancio Philae dovrà provvedere autonomamente al proprio funzionamento. Per questo motivo su di esso vi è una batteria primaria non ricaricabile di 1000 Wh ed una secondaria di 130 Wh alimentata da una serie di pannelli presenti sulle superfici del lander.
La fase operativa di prima ricerca scientifica (FSS) della durata di 5 giorni cometari (circa 60 ore) è garantita dalla batteria primaria, mentre per l'estensione della missione si fa affidamento sul funzionamento dei pannelli solari. I 6 pannelli solari hanno un estensione di 1.4 m^2 e sono composti da 1224 celle solari a bassa intensità e bassa temperatura (LILT). Il sistema produrrà una potenza totale di 8 W, che verrà incanalata su un bus di 28 V attraverso un sistema di 5 MPPT (Maximum Power Point Tracker).

Le celle solari di Philae Le celle solari sono state progettate per funzionare a temperature attorno ad i -160°C e a intensità solari pari a 0.11 SC. La loro grandezza è di 33.7 x 32.4 mm e lo spessore 200 μm. Alla temperatura di 25°C e sotto un illuminazione pari a 1 SC si ottiene una tensione V_{oc} attorno ai 640 mV e una corrente I_{sc} attorno a 520 mA, per temperature ed intensità inferiori la tensione aumenta, mentre la corrente diminuisce.

Apparato sperimentale Per definire le prestazioni delle celle solari è fondamentale ricostruire la curva I-V (corrente tensione). Per questo motivo si è andati a costruire una serpentina sulla quale vi è appoggiata la cella per farla raffreddare, una scheda elettronica che riceva i valori di tensione e corrente per mandarli al computer e tramite un file matlab ricostruire la curva.

La basetta e la serpentina di raffreddamento La serpentina è costituita da due parti tenute insieme tramite 15 viti e bulloni. Entrambe le parti sono state lavorate con macchine utensili in modo tale che congiungendole si crei una serpentina tra le due parti, inoltre all'estremità di una di esse è stata creata una superficie apposita per appoggiare la serpentina, denominata basetta della cella, le sue grandezze sono leggermente più grandi di quelle della cella, inoltre vi è una scanalatura per i cavi della termocoppia in modo da sapere a che temperatura si trova la cella. Le dimensioni finali di essa sono 80 x 70 x 18 mm ed il materiale è rame che è un ottimo conduttore

termico.
La serpentina verrà poi collegata alla bombola di azoto liquido in modo da ottenere temperature sotto i -100°C.

La scheda elettronica Per ricreare la curva I-V e trasmettere i dati al computer è stata costruita una scheda elettronica, la quale è attaccata ad una scheda di acquisizione dati per immagazzinare i dati e gestire le operazioni tramite un programma apposito al computer: Matlab affiancato a Simulink.
La scheda è composta principalmente da amplificatori, resistenze, condensatori e switches.
L'idea che ci sta dietro è quella di creare un cortocircuito in cui si ha corrente massima e tensione nulla, poi chiudendo il circuito si inizia a caricare dei condensatori in modo da diminuire la corrente ed aumentare la tensione fino ad avere corrente nulla e tensione massima, in questo modo si ripercorrono tutti i punti della curva I-V.
La gestione della simulazione è controllata tramite un file in matlab che fa partire un file di Simulink, al suo interno sono gestiti i tempi di apertura e chiusura degli switches per far partire la raccolta dei dati, infine con matlab vengono ricreate le curve tensione-corrente.
Durante la realizzazione di essa sono stati riscontrati diversi problemi, per questo motivo sono state fatte delle prove sugli amplificatori operazionali e si è scoperto che per la corrente non lavorano linearmente.

Test Per vedere l'effettivo funzionamento della scheda elettronica sono state effettuate delle prove in laboratorio a temperatura ambiente. Per l'illuminazione della cella si è utilizzata una semplice lampadina a filo incandescente, spostando la distanza della lampadina dalla cella era possibile cambiare l'intesità di illuminazione della cella.
I risultati finali mostrano il reale andamento della curva I-V ma con un po' di problemi. Il primo riguarda i punti di partenza, i quali non partono dall'asse delle ordinate, ma sono spostati verso destra, questo problema è causato dalle resistenze interne alla cella e dalle resistenze in serie ai condensatori.
Il secondo problema riscontrato sono i vari disturbi i quali fanno formare la curva I-V da più punti sparsi, quindi la curva è più spessa.
Un altro test che si è andati a fare è sulla corrente scura, la cella è stata inserita in una camera scura, quindi senza nessuna fonte di illuminazione, si è poi andati ad alimentare una tensione sempre maggiore nella cella, fino a vedere ad un certo punto che la cella iniziava a trasmettere una certa corrente.

Conclusione e sviluppi futuri Questa tesi mostra le basi per la creazione di un apparato sperimentale per la caratteizzazione delle celle solari in ambiente LILT, con la creazione di una serpentina più basetta per il raffreddamento delle celle solari, i cui test effettuati mostrani il buon funzionamento di essa, inoltre la creazione di una scheda elettronica in grado di ricostruire la curva I-V delle celle solari.
Questa tesi è un punto di partenza, gli steps fondamentali per creare un apparato sperimentale e i tests da fare sono elencati qui di seguito:

- Progettazione e costruzione della basetta e della serpentina di raffreddamento: entrambi realizzati all'interno di questa tesi.
- Progettazione e costruzione della scheda elettronica per ricreare la curva I-V: realizzata all'interno di questa tesi, anche se ulteriori tests e miglioramenti devono essere ancora effettuati.
- Progettazione e realizzazione del box per le prove: questo elemento che deve essere ancora realizzato è molto importante per effettuare prove sperimentali a basse temperature, poiché bisogna ricreare un ambiente chiuso per non avere problemi di condensazione sulla cella, e bisogna fare in modo che la cella riceva luce solo dalla lampada.
- Lampada solare: bisogna costruire o comprare una lampada che abbia lo stesso spettro del sole, inoltre ad essa bisogna applicare dei filtri per avere un'intensità solare più bassa.
- Tests a temperatura ambiente: servono per vedere se la scheda funziona correttamente.
- Tests in condizioni LILT a BOL: i risultati servono per essere confrontati con i risultati già esistenti.
- Tests in condizioni LILT a EOL: le celle devono essere invecchiate artificialmente, dopodicé è possibile effettuare tali tests, essi sono molto importanti poiché non sono mai stati effettuati sulle celle solari di Philae.
- Tests con la presenza di ombreggiamento.
- Tests con la presenza di polvere sulla cella: dato che non si conoscono bene le condizioni ambientali sulla cometa è possibile che sui pannelli si formino dei residui di polvere.

Chapter 1

Introduction

During the last twenty years, there has been a very fast progress in the development and production of high efficiency space solar cells, thanks to the replacement of the silicon solar cells with the multi-junction solar cells, the efficiency of solar cells actually increased by more than 50% from the beginning of nineties to today.

Photovoltaic solar cells were initially used for Earth orbiting spacecrafts and, successively, for interplanetary mission. In deed, they were developed to solve the problems linked to the use of the Radioisotopes Thermoelectric Generators (RTGs). The use of photovoltaic power is now required during the launch for safety reasons and because of the new international norm for environment protection that limits the use of RTGs. As a consequence, the activity on photovoltaic cells has largely increased and particularly on those working in Low Intensity and Low Temperature (LILT) conditions.

The first mission of the NASA discovery program, the NEAR (Near Earth Asteroid Rendezvous) was the first solar-powered spacecraft to fly beyond the orbit of Mars at a distance of 2.2 AU; indeed, this occurred thanks to the use of GaAs (Gallium Arsenide) single junction solar cells. The NEAR mission was launched in 1996 and ended in 2001.

In 2002, an other important NASA exploration mission, Stardust (launched in 1999 and ended in 2011), reached the record of 2.72 AU thanks to the use of silicon solar cells.

The first deep space mission of ESA that employed the photovoltaic power is Rosetta. Rosetta spacecraft has a power generator of only two giant solar panels with a length of 14 m and a total area of 64 m^2; it allows Rosetta to operate as far as 5.25 AU (over 790 million kilometres from the Sun), where the sunlight intensity is less than 4% of the one on Earth and the temperature is lower than -100°C.

The goal of the Rosetta mission is to land on a comet and to perform experi-

ments on it. The studies of comets are crucial to understand the origin of the solar system. Indeed, comets are originated together with the Sun and planets, but, in contrast to them, they have not changed since then and, therefore they carry a message from the time the planetary system was formed, i.e. 4.5 billion years ago.
Given the inverse square decrease of solar intensity with the solar distance, in order to operate at far distance, it is necessary to build a relatively large photovoltaic power system. As shown in Figure 1.1, it is possible to consider the LILT area as the region starting from the orbit of Mars and delimited by the orbit of Jupiter.

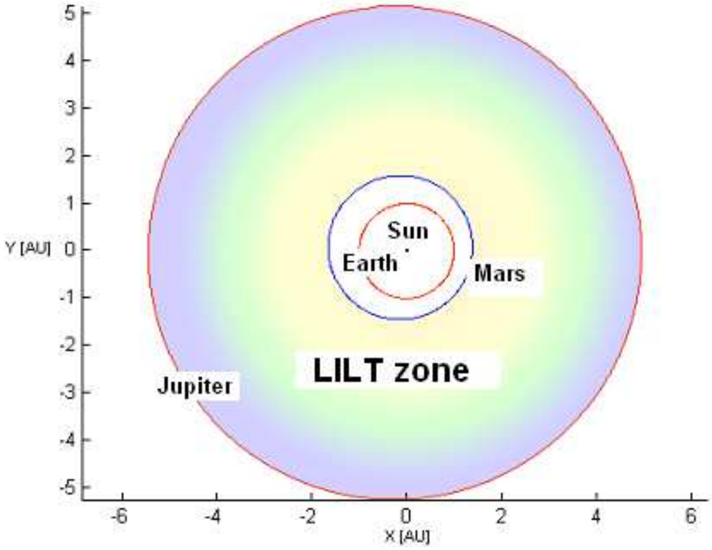

Figure 1.1: Graphic representation of the LILT area [1].

For the Rosetta mission and future mission is important to understand how the LILT solar cell work, for example when there are problems of shading or dust on the cells. For this reason is important to recreate in laboratory a space ambient, with low temperature and solar intensity very low. The scope of this thesis is to create an experimental equipment that is able to cooling a single solar cell to temperature around -100°C, and to create an electronic board able to take the values of voltage and current from the cell and send all the data to a computing environment for crate the I-V curve. This is the first step for crate a complete experimental equipment for characterization the LILT solar cells.

Chapter 2

Photovoltaic effect

The working principle of the solar cells is the photovoltaic conversion, that converts the energy of light directly into electricity.
The first experiment on the photovoltaic effect dates back to the 1839, when the French physicist *A. E. Becquerel* (1820-1891) experimented the first prototype of photovoltaic cell. In 1888 Russian physicist Aleksandr Stoletov built the first photoelectric cell based on the outer photoelectric effect discovered by Heinrich Hertz earlier in 1887. But the first practical solar cells was developed only in 1954 by Chapin, Fuller and Pearson.
The solar cells are essentially made of layers of semiconductor materials with different characteristics. The main semiconductor materials of interest for this type of application are solids crystalline consisting of elements of column IV of the periodic table of Mendelejev (silicon and germanium), or binary compounds, consisting of elements of the III and V column (for example gallium arsenide, GaAs).

2.1 Solar intensity

The solar spectrum of irradiation is similar to a blackbody with a temperature around 5778 K [7]. The irradiation of the sun on the outer atmosphere when the Sun and Earth are spaced at 1 AU, that means Earth/Sun distance is 149597890 km, is called the solar constant. Currently accepted values are about 1360 W/m^2 (the NASA value given in ASTM E 490-73a is 1353 ± 21 W/m^2). The World Meteorological Organization (WMO) promotes a value of 1367 W/m^2, in both cases in Air Mass 0 (AM0). This acronym indicates the spectrum after that solar radiation has passed through the atmosphere, in particular the coefficient of 0 indicates the absence of it. The solar constant is the total integrated irradiation over the entire spectrum (the area under the curve in Figure 2.1) plus the 3.7% at shorter and longer wavelengths.

The irradiation falling on the Earth's atmosphere changes over a year by about 6.6% due to the variation in the Earth/Sun distance. Moreover, solar activity variations cause irradiation changes of up to 1%.
The spectrum of the solar radiation outside the Earth's atmosphere is in the range of $200 - 2500$ nm, includes 96.3% of the total irradiation with most of the remaining 3.7% at longer wavelengths. Many applications involve only a selected region of the entire spectrum. Through the Earth's atmosphere, the solar radiation is further modified to phenomena effect of absorption (mainly due to water vapour and ozone) and scattering and, to the ground, only a part of the spectrum AM0 is available for photovoltaic conversion.

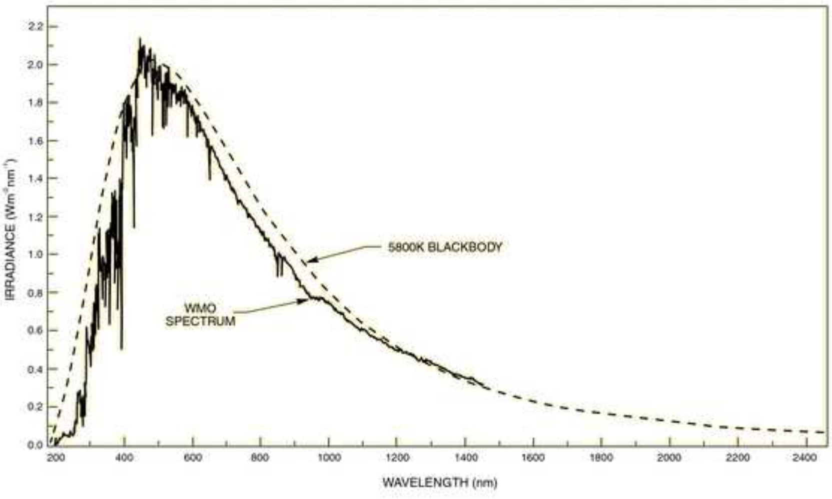

Figure 2.1: Spectrum of the radiation outside the Earth's atmosphere compared to spectrum of a 5800 K blackbody.

2.2 Semiconductor materials

One possible classification for solid materials stands in conductor, isolating and semiconductor. In conductor there is no energy gap between the valence band and conductor band; the electrons can circulate free. In isolating the energy gap is very big, for this reason is not possible to transfer electrons from the band of valence to the conductive. In semiconductor, the energy gap existing between the two bands can be filled with the administering of a suitable quantity of energy. The presence of impurity in material operate a reduction of the energy gap, with the addition of intermediate band acceptatrice or contributor of electrons. This elements are commonly named

“doping elements”, when are injected purposely in the material.
In chemistry a covalent bond involves the sharing of pairs of electrons between atoms. The stable balance of attractive and repulsive forces between atoms when they share electrons is known as covalent bonding. In the case of elementary semiconductors, such as Si and Ge, the tendency to complete the outer shell is realized with the formation of covalent bonds between pairs of identical atoms, in which each atom of the pair puts in sharing one of its four valence electrons to form the bond. Every atom in the crystal forms then four identical bonds with four other identical atoms, sharing with them its electrons. Figure 2.2 shows a diagram of the two-dimensional covalent bonds between the silicon atoms. It is possible to dope the silicon with

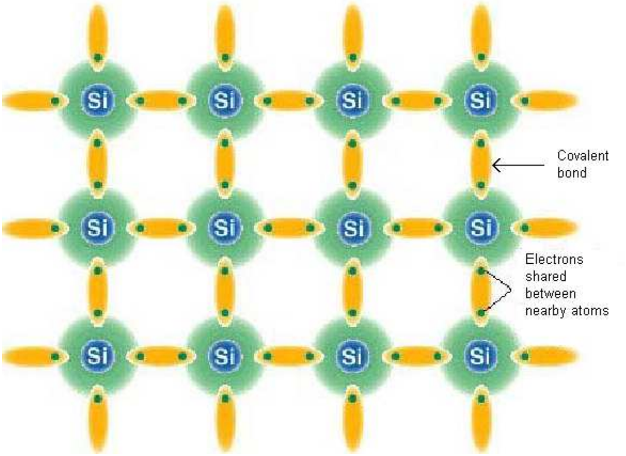

Figure 2.2: Diagram of the two-dimensional covalent bonds between the silicon atoms [15].

boron ($Z = 5$) and phosphorus ($Z = 15$), in order to generate free charge carries, that have negative sign (electrons) or positive sign (holes), that is possible to see in Figure 2.3. When a doped semiconductor contains excess holes it is called “p-type”, and when it contains excess free electrons it is known as “n-type”. The semiconductor material used in devices is doped under highly controlled conditions to precisely control the location and concentration of p- and n-type dopants. A single semiconductor crystal can have multiple p- and n-type regions. When a p semiconductor is coupled with a n semiconductor a p-n junction is generated, they are defined as base and emitter. In the junction region it is created a depletion region, where the free electron in n tends to migrate in p, creating an electric field direct from n to p. If it connects the junction to an external load, a transient current will circulate in the circuit, but will run out quickly. If we want to recreate the effect of “generator” of the junction, it is necessary that the charges flowed

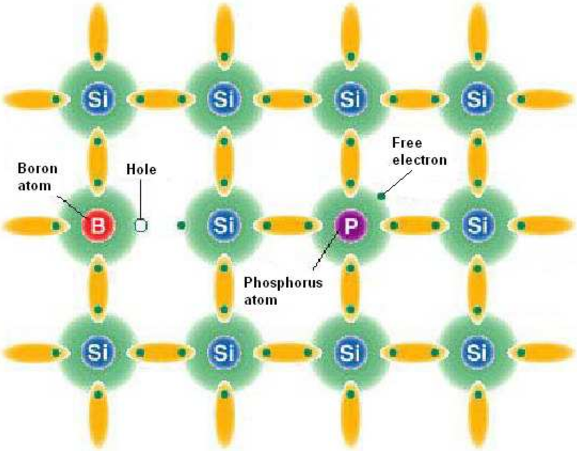

Figure 2.3: Silicon drugged with boron and phosphorus, which generates free charge carriers, that are positive (holes) or negative (electrons) [15].

in the external circuit are restored in the two semiconductors , recreating the initial situation: this happens through the photovoltaic effect.

2.3 Photovoltaic principle

The photovoltaic effect is the creation of voltage or electric current in a material upon exposure to light. When the sunlight or any other light is incident upon a material surface, the electrons present in the valence band of the metallic atom absorb energy and, being excited, jump to the conduction band and become free. Now, these free electrons are attracted by a positively charged electrode and thus the circuit completes and the light energy is converted into electric energy.

2.4 Characteristic of solar cells

If no load is applied to the photovoltaic cell, and it there is no shorting link between the metal contacts duplex, the photovoltaic process shows a voltage of maximum open circuit called V_{oc} at its extremes (in this condition the current in the device is zero). In short circuit condition, however, between the front and back of the cell, we measure a maximum current called I_{sc} with no voltage at the ends.
When there is an external load, the current I_{sc} decreases by an amount equal to the dark current of the cell and in the opposite direction of the one generated by the photovoltaic process. This is because with an external load

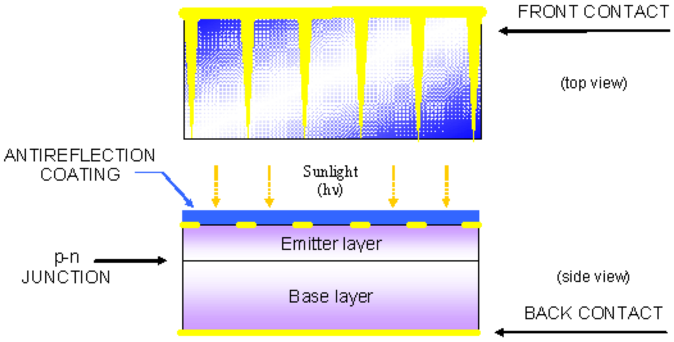

Figure 2.4: Simplified diagram of a solar cell in which are depicted the basic elements [15].

the cell becomes a diode to which is applied a voltage; like this in the cell together with a current generated by the photovoltaic effect, there will also be a diode current. If we choose by convention that the photo current is positive, the total current within the cell is given by the sum of the short-circuit current (I_{sc}) with the dark current (I_d):

$$I = I_{ph} - I_d$$

where I_{ph} is the photo generated current (when a null load is applied corresponds to I_{sc}). The *dark current* is:

$$I_d = I_s \left[e^{\left(\frac{qV}{KT}\right)} - 1 \right]$$

where I_s is the dark current of saturation, K the constant of Stefan Boltzmann, T is the absolute temperature and q the electron charge. The characteristics will be shown in Figure 2.5: here it is possible to locate the point of maximum power, P_{max}, which corresponds to current and voltage maximum power, V_{mp} and I_{mp}, respectively. The *open circuit voltage*, V_{oc}, can be expressed as:

$$V_{oc} = \frac{KT}{q} \log \left(\frac{I_{ph}}{I_s} - 1 \right)$$

An other fundamental parameter is the *fill factor* that show the ratio between the maximum power and the product of open circuit voltage and short circuit current:

$$FF = \frac{I_{mp} V_{mp}}{I_{sc} V_{oc}} = \frac{P_{max}}{I_{sc} V_{oc}}$$

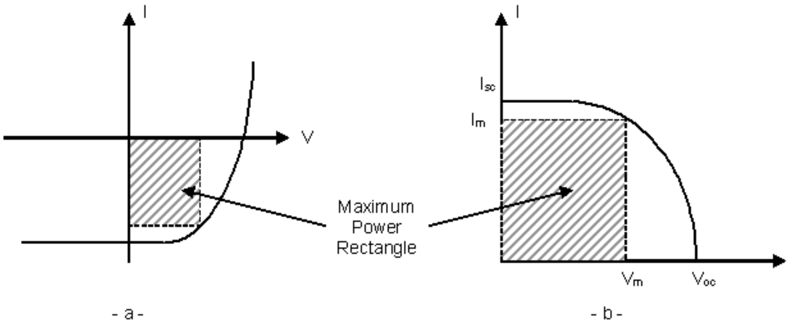

Figure 2.5: (a)Example of I-V curve of a solar cell illuminated. (b) Example of I-V curve in accordance with the generator convention [15].

Finally, it is necessary to take into consideration also the *efficiency* of the solar cell, defined as the ratio between maximum power produced and total power incident on the surface:

$$\eta = \frac{P_{max}}{P_{inc}}$$

There are many factors that limit the efficiency of conversion; the main important concerns the energy-gap. The semiconductor materials characterized by a low value of energy-gap are able to absorb a larger portion of the spectrum of light radiation with respect to the materials of high energy-gap, and therefore they are capable of generating a greater photovoltaic current. Photons with energy lower than the Energy-gap don't generate pairs of electron-hole, while those with higher energy generate only one couple, dissipating the rest in heat. This is one of the limiting factors in the efficiency of conversion. Decreasing the energy-gap also decreases the value of V_{oc} due to the dark current.
Other limiting factors are:

- Optical properties (Egap characteristic, refractive index, absorption) and transport of the material (carrier mobility, life times, lengths of diffusion).
- Cell Structure, thickness and doping of the layers (absorption and generation of carriers).
- Effects of recombination of the carriers before they are collected from the contacts.
- Parasitic resistances.

- Configuring the metal grid.
- Properties of the antireflect layer.
- Level of sunstroke.
- Spectral distribution.
- Operating temperature.
- Effects due to radiation of the space environment.

Figure 2.6 shows the equivalent electrical diagram, in a lumped parameter way, of a solar cell. This is replaced by a constant current generator, I_L, in parallel with the junction, having the symbol of the diode, R_s is the series resistance, R_{sh} is the shunt resistance and R_L the load resistance. When the cell is connected to a load resistor it has a clear passage of current I and a voltage drop V.

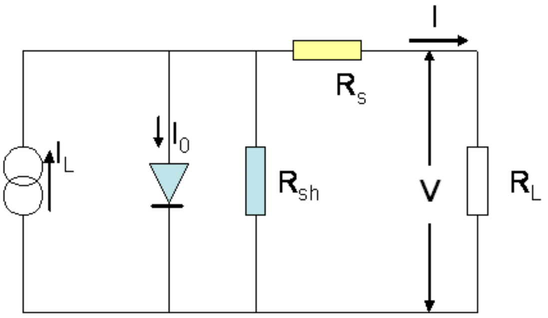

Figure 2.6: Conventional solar cell model with photo current I_L, diode current I_0, shunt resistance R_{sh}, series resistance R_s, output voltage V, output current I and load resistance R_L [29].

A mathematical model con be described with the formula:

$$I(V) = I_{sc} - (I_{sc} - I_m)e^{-\frac{V_m \ln(1-\frac{I_m}{I_{sc}})}{V_m - V_{oc}}}\left(e^{-\frac{V \ln(1-\frac{I_m}{I_{sc}})}{V_m - V_{oc}}} - 1\right)$$

where V_m and I_m are voltage and current at maximum power point.
The photovoltaic current is linearly dependent on the intensity of light incident on the junction: I_{ph} is proportional to the number of carriers generated and hence the number of absorbed photons. In general, the photovoltaic current density generated is expressed with the relation:

$$J_{ph} = \int_0^\infty P(\lambda) Sr_{ext}(\lambda) d\lambda$$

where $P(\lambda)$ is the density of the incident solar power function of the wavelength, while Sr_{ext} is the external spectral response of the material (defined as the ratio between the current produced and the incident power of a monochromatic beam).

2.5 Single junction silicon solar cells

The solar cells of Rosetta have the spectrum showed in Figure 2.4, with a single junction p/n based on silicon. This type of cells allows to obtain a conversion efficiency of around 15% under conditions of AM0 and 25°C of temperature. In Figure 2.7 is possible to see that silicon solar cells absorb the visible part of the solar spectrum ($380 - 700\ nm$) more than infrared portion ($700\ nm$ to $1\ mm$) of spectrum. Crystalline silicon has a energy gap (Eg) of $1.1\ eV$ at $300\ K$.

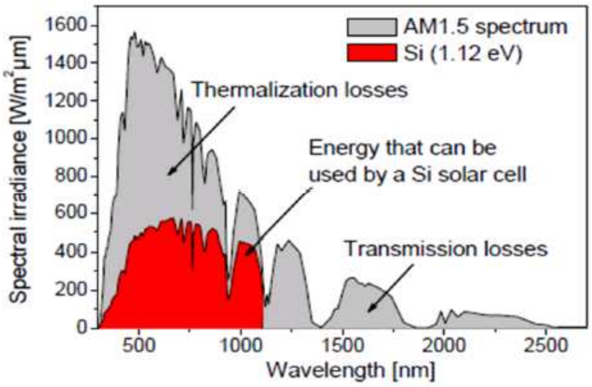

Figure 2.7: Energy that can be used by a silicon solar cell.

2.6 III-V solar cells

The silicon solar cells were preferred until a few years ago for use in space due to their very low cost and because the technology was already developed. Now, however, for address many of the limitations that they were suffering, uses solar cells consisting of group III-V semiconductors such as GaAs, in single or multi junction grown on germanium. This latest technology is of great interest in the field of space due to the high conversion efficiency (that can reach to $28 - 30\%$) and resistance to cosmic radiation.
The multi-junction solar cells are made with the aim to exploit as much as possible across the visible spectrum of light, going to optimize each layer

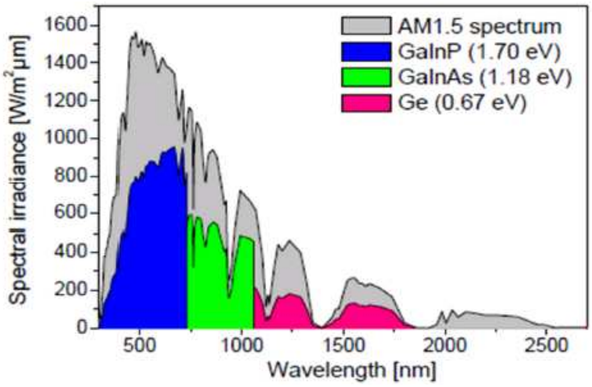

Figure 2.8: Energy that can be used by a triple junction solar cell.

based on the portion of the spectrum absorbed (Figure 2.8). From the studies that are performed by CESI, in around few years they can obtain solar cells with an efficiency of 35%, with a decrease of thickness and costs [18].

2.7 Temperature effects

The maximum conversion efficiency of a solar cell is bounded by the temperature of operation, due to the fact that many of the parameters that are the basis of the photovoltaic device show a temperature dependence.

2.7.1 Energy-gap

An increase of the temperature corresponds to a lower value of energy gap due to an increase of the motion of agitation of atoms. The mean interatomic distance increases and the electrons see a minor potential; as a consequence, the allowed energies are lower. However, as the temperature increases, the open circuit voltage shows a rapid decrease due to the exponential dependence of the saturation current on the temperature (which increases the denominator) and by the Energy-gap in accordance with the relation:

$$I_s \propto e^{-\frac{E_{gap}}{KT}}$$

If the deterioration of fill factor is added to this effect, the outcome is a degradation of the efficiency [2].
The energy gap (E_g) for most of the semiconductors has a decreasing trend with the temperature. It can be described by two equations depending on

the materials. For: Ge, Si, GaAs, InGaAs and AlGaAs it is

$$E_g(T) = E_g(0) - \frac{AT^2}{(T + B}$$

while for InGaP, AlInP and AlInGaP it is

$$E_g(T) = E_g(300) - A(T - B)$$

where T is the temperature in Kelvin, A and B are two empiric coefficients, $E_g(0)$ and $E_G(300)$ are the energy gaps related to the temperature of 0 and 300 K. The values are reported in Table 2.1.

Table 2.1: Energy gap parameters for the two equations.

Type	$E_g(0)$ $[eV]$	$E_g(300)$ $[eV]$	A$[eV/K]$	B$[K]$
Si	1.165		$7.02e^{-4}$	1108
$GaAs$	1.519		$5.405e^{-4}$	204
$In_{0.015}Ga_{0.985}As$	1.457		$5.405e^{-4}$	204
$Al_{0.8}Ga_{0.2}As$	2.475		$7.880e^{-4}$	302
Ge	0.744		$4.774e^{-4}$	235
$AlInP$		2.572	$4.800e^{-4}$	300
$InGaP_2Disorderly$		1.880	$4.800e^{-4}$	300
$InGaP_2Orderly$		1.835	$4.800e^{-4}$	300
$Al_{0.5}InGa_{0.5}P$		2.209	$4.800e^{-4}$	300

2.7.2 Carrier mobility

The mobility is the proportionality coefficient between the drift velocity of a charged particle and the applied external electric field:

$$\mu = \frac{\nu_d}{E}$$

Mobility is mainly limited by collisions with charged impurities and thermal scattering. The minority carrier can be scattered by lattice atoms in thermal motion and their path can be deflected by the electric field generated in the neighboring of a charged donor or acceptor atom. The first mechanism dominates at high temperatures, while the second one is more incident at low temperature and in high doped material. The overall effect on the mobility can be approximated with the Matthienssen relation:

$$\mu = \left(\frac{1}{\mu_{ph}} + \frac{1}{\mu_i} \right)^{-1}$$

Where the first term represent the thermal scattering and the second the impurity scattering.
Both for the GaAs cells and for the Silicon ones, mobility decreases with increasing doping of the semiconductor, and the temperature dependence becomes less sensitive.

2.7.3 Dark currents and lifetimes

Under operating conditions of solar cells, opposite to the photo generated current is generated a dark current, due to the establishment of a direct bias voltage between its terminals. At the base of the dark current, which goes to deteriorate the performance of the solar cell, there are mainly three mechanisms of transport of carriers through the depletion region: diffusion, recombination and tunnel. The first two are depending on the temperature and the third not (see [15] for more details).
The lifetimes of minority carrier remain approximately constant over the temperature of −50°C, for lower temperatures they drop slightly (for more details see [2]).

2.8 Solar intensity effect

If the temperature is held constant, the current output decreases linearly with decreasing intensity, while the voltage output decreases logarithmically. The photo generated current (J_{ph}), in fact, is directly proportional to the number of incident photons ($F(\lambda)$). As shown in the equation 2.1, this is expressed by the integral over the incident wavelength range of the product between the density of incident photons and the cell quantum efficiency, being this last term the ratio between the number of generate carriers and the number of incident photon per unit wavelength.

$$J_{ph} = q \int_0^{\infty} F(\lambda) QE(\lambda) d\lambda \tag{2.1}$$

While the open circuit voltage depends on the short circuit logarithm.
At lower solar insolation the leakage current becomes comparable with the photo generated current and the shunt resistance assumes considerable importance, reducing the Fill Factor and the output voltage.

2.9 Possible causes of performance loss in LILT conditions

Solar cells which exhibit good performance in AM0 condition may have a significant loss in fill factor, and thus in the power generator, in LILT conditions.
This loss in fill factor is mainly due to two effects which show up under low intensity and low temperature conditions: respectively the shunt effect and the flat spot phenomena. The way these features affect the solar cell I-V characteristic at LILT conditions is showed in Figure 2.9. The Flat Spot is revealed as a triple slope in the IV curve (Broken-Knee), and its origin is associated with a particular type of defect called Metal Semiconductor Like.

The shunt is a preferential path parallel to the junction for the current crossing the cell. Those paths can be caused by:

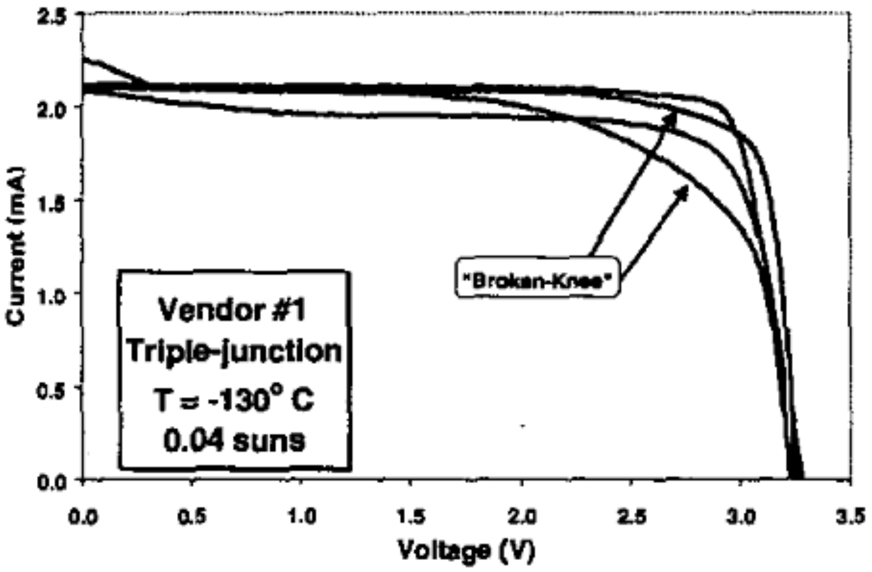

Figure 2.9: Typical LILT degradation phenomena can become apparent under LILT measurement conditions.[19]

- Crystal defects on the surface of the cell which enable metal intrusion in the semiconductor from the metallization.
- Edge effects: typically defects created on the cell edge during the cell cut.
- Crystal defects that activate below a certain current density flow.

- Doping diffusion from the tunnel layers.
- An excess of doping in the emitter or base layers.

2.10 Radiation damage

In an environment such as space, solar cells interact with particles with mass, high energy and possibly charge, such as electrons, protons, neutrons and ions.
When one of these particles is absorbed by a material in general may occur several phenomena of interaction between the particle energy and the atomic structure of the material [20].
The dominant interactions are:

- Inelastic Collisions with Atomic Electrons. Inelastic collisions with bound atomic electrons are usually the predominant mechanism by which an energetic charged particle loses kinetic energy in an absorber. In such collisions, electrons experience a transition to an excited state (excitation) or to an unbound state (ionization).
- Elastic Collisions with Atomic Nuclei. Energetic charged particles may have coulombic interactions with the positive charge of the atomic nucleus through Rutherford scattering. In some cases the amount of energy transferred to the atom will displace it from its position in a crystalline lattice. If sufficient energy is transferred to displace an atom from its lattice site, that atom will probably be energetic enough to displace many other atoms.
- Inelastic Collisions with Atomic Nuclei. Highly energetic protons undergo inelastic collisions with the atomic nucleus. In this process the energetic proton interacts with the nucleus and leaves the nucleus in an excited or activated state. The excited nucleus emits energetic nucleons and the recoiling nucleus is displaced from its lattice site.

2.10.1 Ionization

The main types of radiation damage in solar cells are mainly due to ionization and displacement of atoms.
The ionization occurs when an electron in the outermost orbital is removed from the atom. To quantify the ionization radiation refers to the dose of radiation absorbed by the material, expressed in rad (1 erg/g or 0.01 J/Kg). In this way different radiation exposure can be traced to the absorbed doses,

reflecting the damage suffered by ionization in the material of interest. For the electrons absorbed, the dose is calculated from the incident fluence ϕ $[e/cm^2]$ (particles through the unit area integrated for a certain time).

$$Dose(rad) = 1.610^{-8}\frac{dE}{dx}\phi$$

where $\frac{dE}{dx}$ $[\frac{Mev \cdot cm^2}{g}]$ is the electron stopping power in the material of interest. This concept can be applied to electron, gamma and X-ray radiations of all energies, while for the protons only for those producing a homogeneous damage in the material, given that protons generally cause a damage localized in the vicinity of the track of the particle.
The main effect of ionization is the reduction of the coefficient of light transmission of cell's coverage; the blackening is due to formation of color centering in the protection, and caused by excitation of electrons in the conduction band which end up trapped impurities in the atomic lattice. Other effects caused by the ionization radiation may be leakage currents in the cell.

2.10.2 Atomic displacements

The atomic displacement is caused by the collision of fast particles in the crystal lattice, so atoms are moved by their position in the lattice, which gives rise to defects and imperfections that produce significant changes in the equilibrium carrier concentrations and a minority carrier lifetime.
The dislocation of the atoms requires a certain minimum amount of energy. When an incident particle has an energy equal to or greater than this threshold, the dislocation can be estimated with the following relationship:

$$N_d = n_a \sigma \bar{\nu} \phi$$

where N_d is the number of displacements per unit volume, n_a the number of atom per unit volume of absorber ($5 \cdot 10^{22}$ silicon atoms$/cm^3$), σ the displacement cross section (cm^2), $\bar{\nu}$ the average displacements per primary displacement and ϕ the radiation fluence ($particles/cm^2$).

2.10.3 Electron displacement damage

In the case of dislocation due to the electron it is possible to found in the lattice gaps whose distribution is not uniform. In fact the gaps left by secondary dislocations lie relatively close to the primary gaps generated from the initial impact with the high energy particle.
In n-type silicon, it has been shown that vacancies react with oxygen impurities to form close coupled vacancy-oxygen pairs, and with impurity donor

atoms, such as phosphorus and arsenic, to form close coupled vacancy-donor pairs. Both defects are electrically active and can become negatively charged by accepting an electron from the conduction band.

2.10.4 Proton displacement damage

The displacement generated by the protons is considerably different because the displacement cross sections are several orders of magnitude larger than those for fast electrons and vary rapidly with proton energy.
The dislocation caused by the proton is highly inhomogeneous, since the many secondary dislocations occur near the site of the primary dislocation.

2.10.5 Neutron displacement damage

In the case of the neutron Coulomb forces are not involved but a collision of the rigid type occurs. The value of cross-section of displacement is smaller than those of the electron and the proton, and this means that the number of primary dislocations is smaller. In addition, the energy is transferred in support of the reformation of the bonds between the atoms of the crystal structure. The main importance of the displacement defects produced by the irradiation of silicon solar cells is in their effect on the minority carrier lifetime of the silicon. In particular, the lifetime in the bulk p-type silicon of an n/p solar cell is the major radiation sensitive parameter.

Table 2.2: Typical values of cross section dislocation in the silicon

	Cross section dislocation
Electron 1 MeV	$68 \cdot 10^{-24} cm^2$
Proton 1 MeV	$3.5 \cdot 10^{-20} cm^2$
Neutron 1MeV	$2.4 \cdot 10^{-24} cm^2$

Chapter 3

Rosetta mission

The Rosetta mission is designed to obtain the most detailed study of a comet ever attempted. To reach this pourpose the Rosetta space probe is associated to a lander, named Philae, which will attempt to make the frst-ever controlled landing on a comet.
The Rosetta mission was approved in 1993 by European Space Agency (ESA) Science Programme Committee, and it is one of the most important mission of the Horizon 2000 program.
In the original mission plan Rosetta was set to be launched in January 2003 to rendezvous with the comet 46P/Wirtanen, and to enter in orbit around it, in 2011. However, in December 2002 the planned launch vehicle Ariane 5 turned out to be a failure. Therefore a new plan was made to target another comet, the 67P Churyumov–Gerasimenko (67P/CG), with launch on 2 March 2004 and rendezvous in 2014.
The mission name is taken from the Egyptian town of Rashid, or Rosetta, where, in 1979, archaeologists found a stone carrying inscriptions in three different ancient languages. Archaeologists were able to decipher them thanks to the help of similar scripts on an obelisk from the town of Philae; the spacecraft's lander has thus been named "Philae". Indeed, space-scientists of Rosetta mission wish to be as well successful as archeologists of Rosetta stone in deciphering the data gathered from the 67P/CG comet [37].
Rosetta mission is principally aimed at studying

1. the origin of comets,
2. the relationship between cometary and interstellar material,
3. its implications with regard to the origin and the evolution of the solar system.

To achieve these goals, the followings milestones (scientific objectives) have been defined: [6]:

- Global characterization of the nucleus, determination of dynamic properties, surface morphology and composition.
- Determination of the chemical, mineralogical and isotopic compositions of volatiles and refractories in a cometary nucleus.
- Determination of the physical properties and interrelation of volatiles and refractories in a cometary nucleus.
- Study of the development of cometary activity and the processes in the surface layer of the nucleus and the inner coma (dust/gas interaction).
- Global characterization of asteroids, including determination of dynamic properties, surface morphology and composition.

3.1 Mission analysis

On 2 March 2004, after the reorganization of the mission due to the problems with the Ariane 5 ECA launcher, Rosetta mission was successfully launched by the Ariane 5 G+ from Kourou in French Guiana. The orbit which has been inserted will bring in about ten years (4,300 days mission) to the comet 67P/CG through a series of fly-by around some system Solar bodies. The timeline of the proposed assignment is described in table 3.1 whereas the Rosetta orbit and the most important points of the mission are reported in Figure 3.1. It is important to note that during the period that Rosetta is orbiting the comet 67P/CG, the latter is going to reach the closest point to the Sun in its orbit.

During the mission period, the variation of the solar intensity is being calculated on the basis of the following equation:

$$S' = \frac{S}{d^2}$$

where “S” is the solar intensity of reference, “d” is the distance of Rosetta spacecraft from the Sun (it is measured in AU), and “S’ ” the relative solar intensity value.

The expected values of distance between the Sun and Rosetta at different time-points of the entire mission period and the relative solar intensity values are reported in Figure 3.2 and in Figure 3.3.

Moreover, Figure 3.4 shows the trend of the solar intensity in SC for the period of operation of the Philae lander. At the beginning of Philae mission, the comet will be located between Mars and Jupiter orbits, so that the detected solar intensity values will be the lowest; instead, in a more advanced

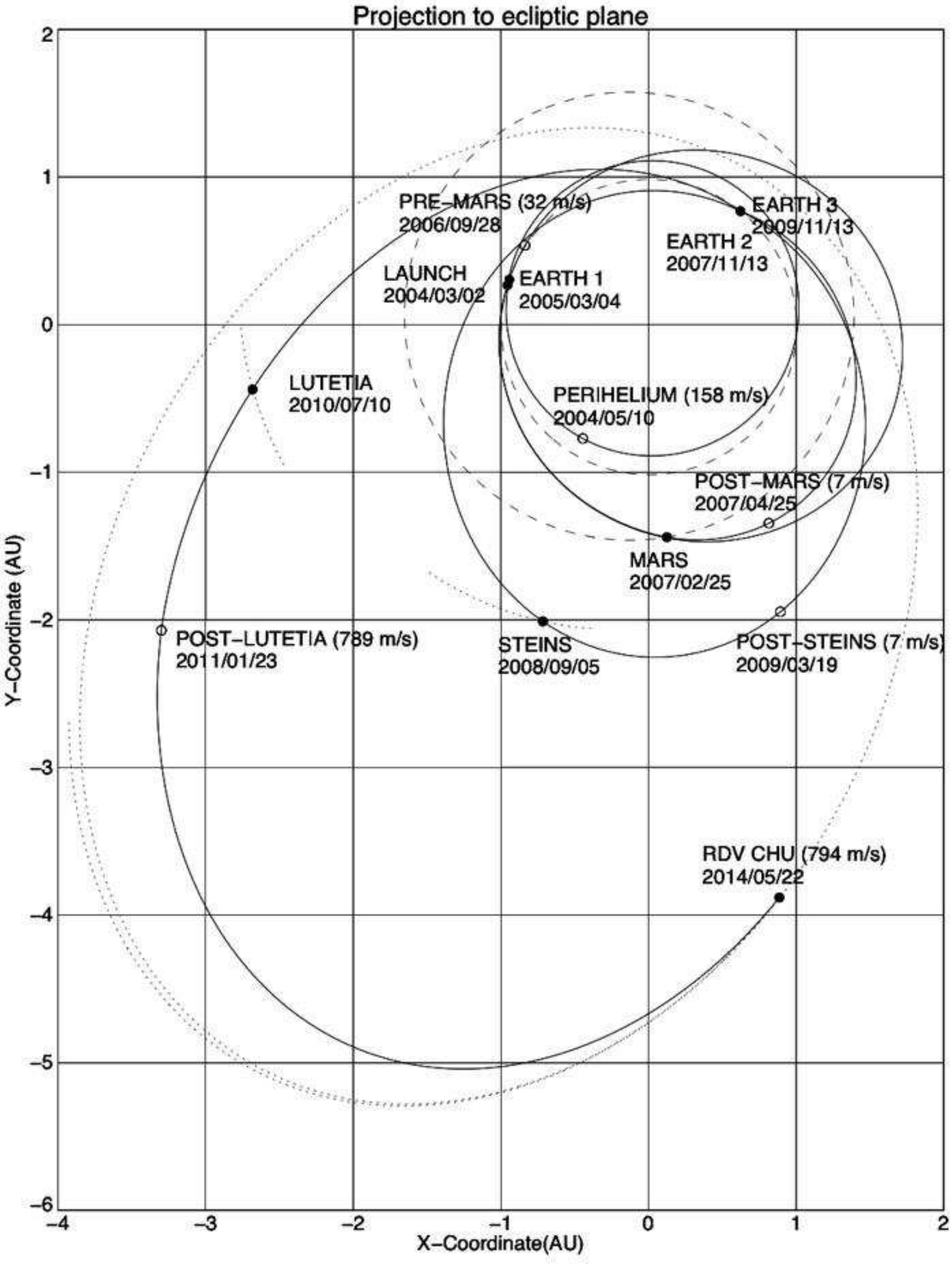

Figure 3.1: Graphical representation of the orbit of Rosetta [3].

Table 3.1: The mission falls into several distinct phases [3].

Event	Nominal date
Launch	2 March 2004
First Earth gravity assist	4 March 2005
Mars gravity assist	25 February 2007
Second Earth gravity assist	13 November 2007
Asteroid 2867 Steins flyby	5 September 2008
Third Earth gravity assist	13 November 2009
Asteroid 21 Lutetia flyby	10 July 2010
Rendezvous manoeuvre 1	23 January 2011
Enter deep space hibernation	July 2011
Exit deep space hibernation	January 2014
Rendezvous manoeuvre 2 between 4.5 and 4.0 AU	22 May 2014
Start of near-nucleus operations at 3.25 AU	22 August 2014
Lander Philae Delivery	10 November 2014
Start of comet escort	16 November 2014
Perihelion Passage	August 2015
End of nominal Mission	31 December 2015

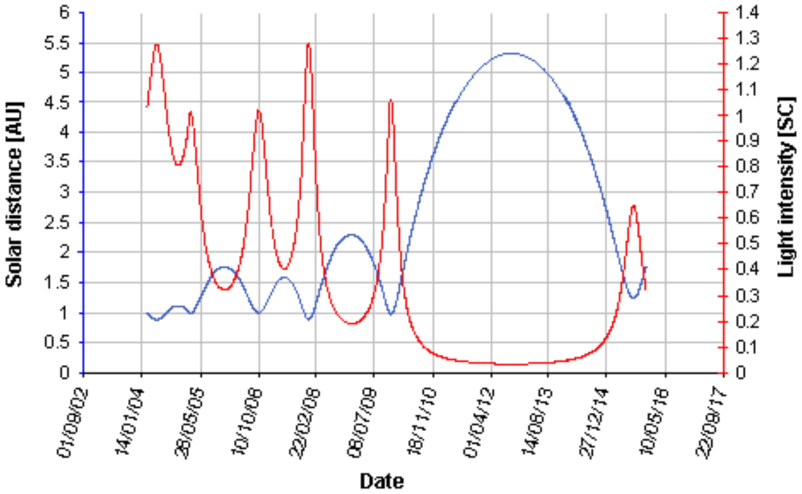

Figure 3.2: Trend of the distance between Rosetta and the Sun, and the light intensity [1].

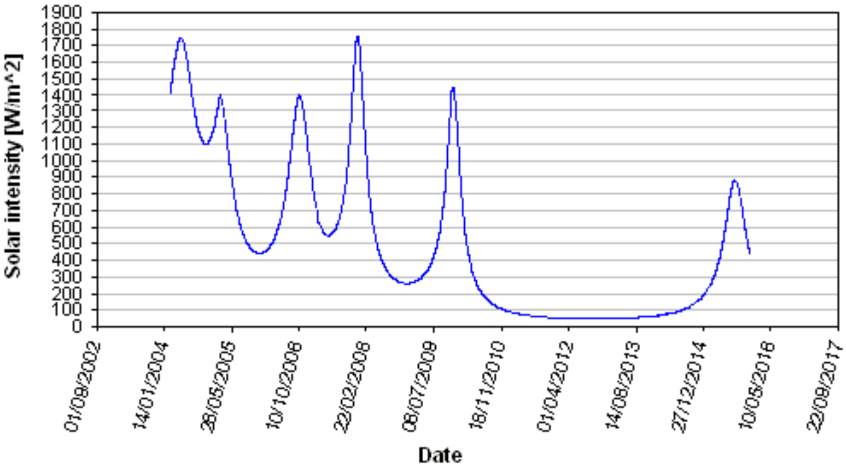

Figure 3.3: Trend of the solar intensity in W/m^2 on Rosetta spacecraft during all the mission time [1].

phase of the Philae mission, the comet will be positioned between Mars and the Earth orbits, corresponding to its perihelion period, thus reaching its maximum values of solar intensity.

The minimum and the maximum solar intensity values that the lander

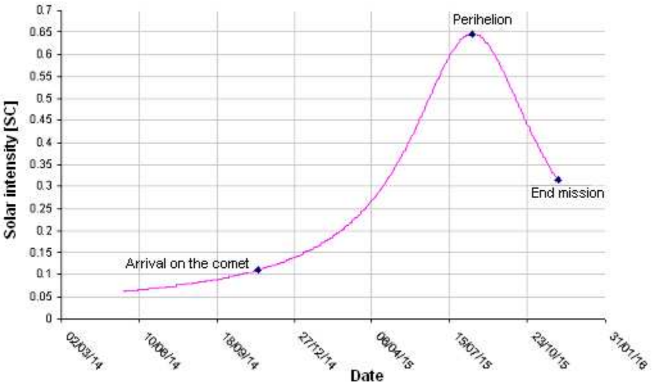

Figure 3.4: Trend of the solar intensity in SC for the period of operation of Philae on the comet [1].

would detect during the mission period are illustrated in Figure 3.2. It is important to consider that during the perihelion phase of its orbit, which is expected in 2015, the comet 67P/ CG would be closest to the Sun than during its previous perihelion phase in 2002: i.e 1.2433 AU instead of 1.29

AU.

Table 3.2: Minimum and maximum solar intensity during the Philae period on the comet.

	Date	SC	Intensity [W/m^2]	Sun distance [AU]
Min	11/11/2014	0.11102	151.87	3.0013
Max	13/08/2015	0.64695	885.03	1.2433

3.2 The comet

3.2.1 What is a comet

Comets are small, fragile, irregularly shaped bodies composed mostly of a mixture of water ice, dust, and carbon- and silicon-based compounds. They have highly elliptical orbits that repeatedly bring them very close to the Sun and then swing them into space. Comets have three distinct parts: a nucleus, a coma, and a tail. The solid core is called the nucleus, which develops a coma with one or more tails when a comet sweeps close to the Sun. The coma is the dusty, fuzzy cloud around the nucleus of a comet, and the tail extends from the comet and points away from the Sun. The coma and tails of a comet are transient features, present only when the comet is near the Sun [8].

3.2.2 Characteristics of 67P/CG

The comet 67P/CG was discovered in 1969, when several astronomers from Kiev visited the Alma-Ata Astrophysical Institute to conduct a survey of comets. On 20 September, Klim Churyumov was examining photographs of comet 32P/Comas Solá taken by Svetlana Gerasimenko when he found a comet-like object near the edge of the plate. He assumed that the faint object was the expected periodic comet, but upon returning to Kiev, he studied the plates very carefully and eventually realized that a new comet had been found, less than two degrees from comet Comas Solá.

The comet has a particularly unusual history. Up to 1840 its perihelion distance was 4.0 AU (four Sun-Earth distances or about 600 million km) and the comet was completely unobservable from Earth. That year, a fairly

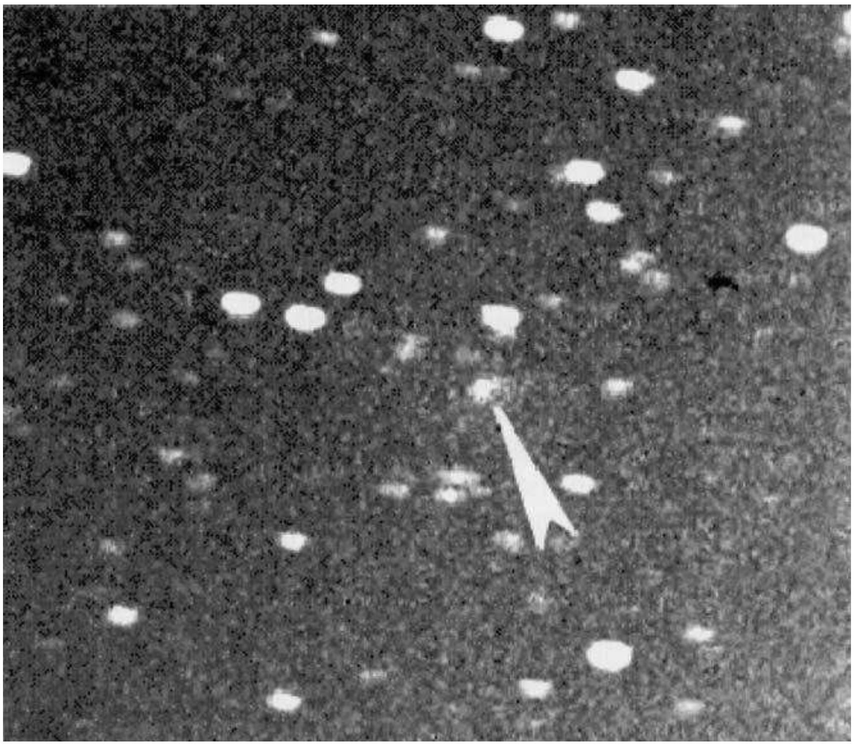

Figure 3.5: Discovery image of comet 67P/Churyumov–Gerasimenko in 1969 [9].

close encounter with Jupiter caused the orbit to move inwards to a perihelion distance of 3.0 AU (450 million km). Over the next century, the perihelion gradually decreased further to 2.77 AU. Then, in 1959, a further Jupiter encounter reduced the perihelion to just 1.29 AU. It currently completes one orbit of the Sun every 6.57 years.

The comet has now been observed from Earth on six approaches to the Sun - 1969 (discovery), 1976, 1982, 1989, 1996 and 2002. It is unusually active for a short period object and it has a coma (a diffuse cloud of dust and gas surrounding the solid nucleus) and often a tail at perihelion. During the 2002/2003 apparition, the tail was up to 10 arcminutes long as seen from Earth, with a bright central condensation in a faint extended coma. Even 7 months after perihelion the tail continued to be very well developed, although it subsequently faded rapidly.

The comet typically reaches a magnitude around 12, although this is because the comet has outburst at perihelion at three of its last four returns in 1982/83, 1996/97 and 2002/03. Despite being a relatively active object, even at the peak of outburst the dust production rate is some 40 times lower than for 1P/Halley. Nevertheless, 67P/CG is classed as a dusty comet.

The peak dust production rate in 2002/03 was estimated at approximately 60kg per second, although values as high as 220kg per second were reported in 1982/83. The gas to dust emission ratio is approximately 2.[6]
Sixty-one images of comet 67P/CG were taken with the Wide Field Planetary Camera 2 on board the Hubble Space Telescope (HST) on 11-12 March 2003. The HST's sharp vision enabled astronomers to isolate the comet's nucleus from the coma. The images showed that the nucleus measures five by three kilometres and has an ellipsoidal (rugby ball) shape. It rotates once in approximately 12 hours. It is composed of a highly porous mixture, in certain percentages of ice of water (the main component), CO_2, CO, carbon compounds, nitrate and silicate dust. The main characteristic of the 67P/CG comet are reported in the Ttable 3.3.

Table 3.3: Comet 67P/CG parameters [6].

Comet 67P/Churyumov-Gerasimenko	
Diameter of nucleus - estimated (km)	3 x 5
Rotation period (hours)	$\sim$ 12
Orbital period (years)	6.57
Perihelion distance from Sun (million km)	194 (1.29AU)
Aphelion distance from Sun (million km)	858 (5.74AU)
Orbital eccentricity	0.632
Orbital inclination (degrees)	7.12
Year of discovery	1969
Discoverers	Klim Churyumov and Svetlana Gerasimenko

3.2.3 The nucleus

The evolution of the nucleus is governed, first, by heat transfer due to conductive and radiative transfer, and second, by exchange of latent heat due to the motion of the gas through the porosity, and heat received through the surface in dependence on its thermo-optical properties (such as albedo and emissivity), in particular by the percentage coverage of the crust of dust, and by the distance of the Sun.
At the beginning of its life, the comet's nucleus can be described as a simple and homogenous body. Instead, during the approach to the Sun, the energy

input through the surface increases the temperature and the ice begins to sublimate, the first component that begin to sublimate is CO, followed by CO_2, while H_2O requires higher temperatures. The sublimation of the ice allows the expulsion of dust particles from the nucleus, or their return on the surface, this depending on the forces into play. All these mechanisms lead to the formation of crust of dust and to the differentiation of substrates. Under the crust, which may or may not be present in different percentages, still persist a homogeneous nucleus [1].

3.2.4 Study of the comet

Following the designation of the 67P/CG comet as the new target of Rosetta mission, space-scientists started to study the physical, geometrical and chemical characteristics of that comet. The most important observations they made are listed below:

- European Southern Observatory and Very Large Telescope (VLT) at La Silla in Chile, between 11 February 2003 and 26 June 2003: spectrum measurements - photometry to determine the rate of production of gas and dust.
- Hubble Space Telescope (HST), January 2003: observations to determine the nucleus (assumed value of albedo), the rotation period and the color index.
- Spitzer Space Telescope : observations to determine the thermal emission of the comet 67P/CG. These measurements combined with those in the visible allowed the use of the radiometric techniques to derive the size and the albedo (correlated which is correlated with the estimate of the first.
- European Southern Observatory with the New Technology Telescope (NTT), 3.5 m (2005): Photometry in the visible to measure the period of rotation, the effective radius, the phase function and the color.

3.2.5 Radiation on the comet

Radiation may be defined as the emission and propagation of energy through free space or through a material medium. The space radiation environment is composed of cosmic rays, electromagnetic radiation, Van Allen belt radiation, auroral particles, and solar flare particles.

The study of radiation is critical for determining the electrical behavior of the Solar cells; in fact, the radiation causes strong degradation which is dependent on the type of radiation encountered and on the residence time in a given area of space.

Radiation in interplanetary space consists of an energetic cosmic flux and pulses of radiation associated with solar flares. In addition to these sources of interplanetary radiation, there also exist a continuous ejection of low energy particles from the sun (primarily protons and electrons) known as the solar wind. The distribution of the solar wind particles is assumed to obey the inverse-square law with the sun acting as a point source.

Cosmic rays of galactic origin consist of protons ($\sim$ 93%) and alpha particles ($\sim$ 7%) along with smaller amounts of heavier elements. Proton (p^+) is a positively charged particle of mass number 1 (having a mass of 1.672 x 10^{-27} kg) and a charge equal in magnitude to the electron (i.e. 1.602 x 10^{-19} coulombs); it is also the nucleus of a hydrogen atom. Alpha particle (*alpha*) is a positively charged particle identical to all properties of the nucleus of a helium atom, consisting of two protons and two neutrons. The energy of the protons is in the range of 5 x 10^8 eV to 2 x 10^10 eV. Although energies are quite high, the free space flux of particles is 2.5 particles pro $cm^{-2}s^{-1}$. Since this flux is small, radiation damage due to cosmic rays usually needs to be considered only on very long space flights [5].

3.2.6 Dimensions and shape

In order to determine the size and shape of the nucleus of the comet 67P/CG, astronomers have performed multiple visual observations of the comet with the Hubble Space Telescope (HST) and the New Technology Telescope (NTT), and also infrared observations with the Spitzer Space Telescope (SST). The size and shape have been then obtained by inverse analyses of photometric light curves in function of time.

The measurements made in the visible through HST and NTT first let to the prediction of two independent models of nuclear shape and size under the following assumptions:

1. value of geometric albedo[1] of 0.04
2. coefficient phase[2] of 0.04 mag/deg.

---

[1] The geometric albedo of an object is defined as the ratio of the brightness at $\alpha = 0$ (α phase angle, i.e. the angle between the light source and the observer), and the brightness of an ideal flat surface, completely reflective and diffusive, with the same cross section.

[2] Relative to the phase function $j(\alpha)$ which gives the ratio of the intensity diffuse in the direction of alpha respect to the intensity diffused to $\alpha = 0$

Those models, indeed resulting from a limited amount of information, are the best-fitting from the observations made up to 2006 and predict an highly irregular area for the comet 67P/CG.
Under given constraints of smoothness of surface and inertia matrix (such as rotation about the main axis), the two models of nuclear shape can be represented graphically in three dimensions, one prograde and one retrograde, as shown in Figure 3.6.

According to these models, the rotation period of the comet 67P/CG would be 12.68 ± 0.03 hours and the orientation of the rotational axis would be defined. Indeed, thanks to the observations of the heat flow through the SST, it has been possible to remove the uncertainty of the albedo value, and thereby to obtain a better estimate of the nuclear size of the comet.

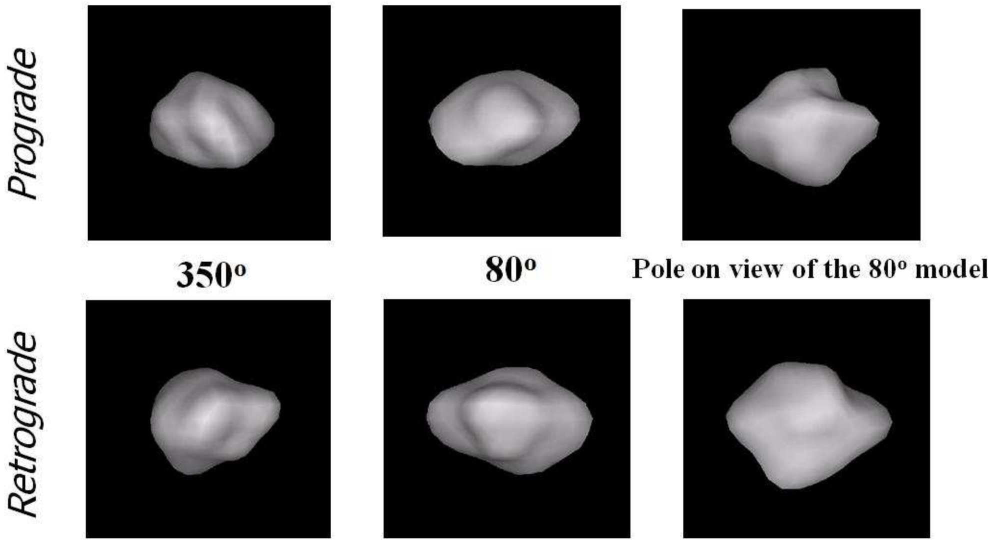

Figure 3.6: The prograde (top row) and the retrograde (bottom row) solutions for the threedimensional shape of the nucleus of comet 67P/CG reconstructed from the inversion of the 2003 HST and 2005 NTT light curves. For each solution, three views of the reconstructed 3-D shape model are displayed at three different rotational phase angles: 350°, 80°, and pole-on view of the 80° model [33].

The Table 3.4 shows the best estimates of physical parameters, obtained from the observations made until 2006. In particular, the density of the nucleus would be in a range between 100 and 500 kg/m^3, with a most likely value of $370 Kg/m^3$. It also provides the moments of inertia and the coefficients of the second degree and order C_{20} and C_{22} harmonic expansion of the gravitational field of the model calculated.

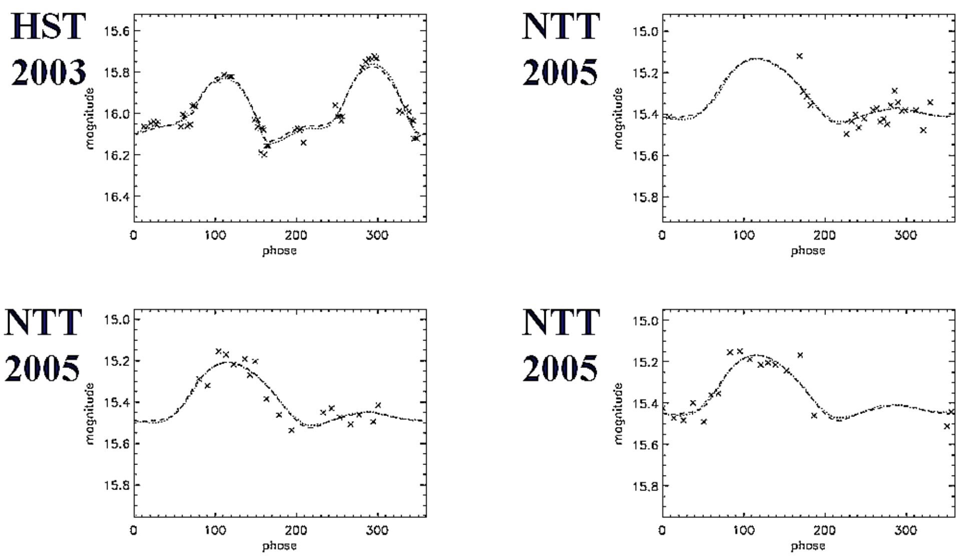

Figure 3.7: Light curves from HST and NNT. The dots represent the recorded data and lines the best-fit for the two solutions [9].

Table 3.4: Principal physical parameters for the comet 67P/CG.

Solution	Prograde	Retrograde
x length	$4.74km$	$4.49km$
y length	$3.77km$	$3.53km$
z length	$2.92km$	$2.93km$
Volume	$21.2km^3$	$21.3km^3$
Area	$40.2km^2$	$40.1km^2$
Mass ($500kg/m^3$)	$1.0e^{13}kg$	$1.0e^{13}kg$
Mass ($100kg/m^3$)	$2.1e^{12}kg$	$2.1e^{12}kg$
Mass ($5370kg/m^3$)	$7.8e^{12}kg$	$7.9e^{12}kg$
Inertia ratio Ix/Iz	0.7	0.67
Inertia ratio Iy/Iz	0.86	0.86
C_{20}	$-0.33/r_0^2$	$-0.35/r_0^2$
C_{22}	$0.060/r_0^2$	$0.060/r_0^2$

3.2.7 Axis of rotation

The nuclear rotational axis of the comet 67/CG has been studied by various astronomers using different techniques .
Each technique used as a starting point some of the constraints that must be met by the resulting light curves and different view geometries observed from the nucleus structure (jets, fans, shells, etc.). To determine the direction of the rotational axis is necessary to provide two angles that can be expressed with respect to the ecliptic coordinates (λ and β), or in terms of right ascension and declination (AR and δ). Maybe the most known hypothesis have been found by Lamy [9] ; through the HST light curves he identified 4 hypothesis, two of which are indeed improbable: the first (likely) hypothesis fits with the prograde solution and identifies $\lambda = 51°\pm20°$ and $\beta = 54°\pm10°$ and corresponds to a clockwise rotation; the second likely hypothesis fits with the retrograde solution and identifies $\lambda = 245°\pm20°$ and $\beta = -50°\pm10°$ and corresponds to an anticlockwise rotation.
Additional likely hypotheses for the nuclear rotational axis of the comet 67/CG have been proposed by Davidsson and Gutiérrez [10]; by using a thermo-physical model and by applying all the constraints inferred by the observations, they have identified two likely intervals for the rotational axis: the first interval is defined by an obliquity (the angle between the spin axis and the angular momentum vector of the cometary orbit) of 120 ° ±30 ° and a topic (the clockwise angle from the point of the vernal equinox of the comet and the subsolar meridian at perihelion) of 60° ±15° ; the second interval is characterized by a skew of 60°±30° and an argument of 240°±15°. Other interesting solutions have been proposed by Chesley (2004), Schleicher (2006) and Weiler (2004) [9].
Taken together the proposed hypotheses led to the idea that the orientation of the rotational axis is included in a region expressed in celestial coordinates $RA = 220°(+50° \ / -30°)$ and $\delta = -70° \pm10°$ (counterclockwise rotation) or in a region expressed in celestial coordinates $AR = 40° \ (+50°/-30°)$ and $\delta = 70°\pm10°$ (clockwise rotation). Figure 3.8 summarizes the so far proposed likely solutions.

3.2.8 Shadow in a crater

The time-window of light availability on the surface of a comet is an important parameter to take in account when landing on a comet. Since comets have craters on their surface, the time-window of light availability is predicted by determining the length of the shadow cast by crater walls [11]; the shadow length is measured on the floor of the depression from the central

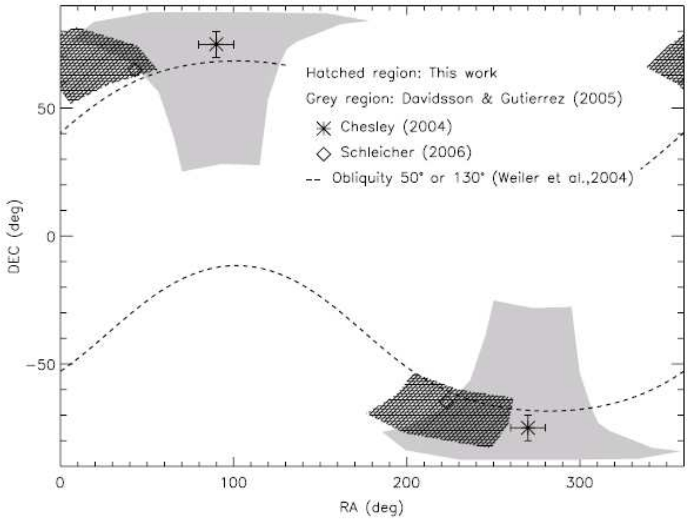

Figure 3.8: Constraints on the direction of the rotational axis of the nucleus of comet 67P/Churyumov-Gerasimenko as determined by different authors [9].

rim to the crater wall along the direction θ, and is currently calculated by using a simple geometric condition resulting in the following relationship:

$$r_{sh} = -z_d \tan\alpha \cos\bigl(\theta - \zeta\bigr) \pm \left(r_d^2 - z_d^2 \tan^2\alpha \sin^2\bigl(\theta - \zeta\bigr)\right)^{0.5}$$

where d_r is the distance from the crater wall to the crater center measured on the floor of the depression, d_z is the crater depth and the angle ζ is the azimuth of the Sun. Here the plus sign indicates the case in which the crater center is illuminated.

3.2.9 Gas production

The measurements made during the 1982 and 1996 apparitions, which occurred when 67/CG was at its perihelion, let to determine the production rate of five gas species: OH (used for calculating the production rate of H_2O), CN, C_2, C_3, and NH. Instead, during the 2002 apparition only a single measurement for the CN has been collected.
As illustrated in Table 3.5, the authors which have contributed to the spectra measurements to assess the gas production rates of 67/CG are many [9].

The production rate of some species can be approximated by the method

Table 3.5: Measurements of production rates by various authors.

Authors and year	Species
Cochran (1992)	CN, C_2, C_3
Storrs (1992)	CN
Osip (1992)	OH, CN
Schleicher (2006)	OH, CN, C_2, C_3, NH
Hanner (1985), Crovisier (2002), Makinen (2004)	OH
Weiler (2004), Schulz (2004)	CN

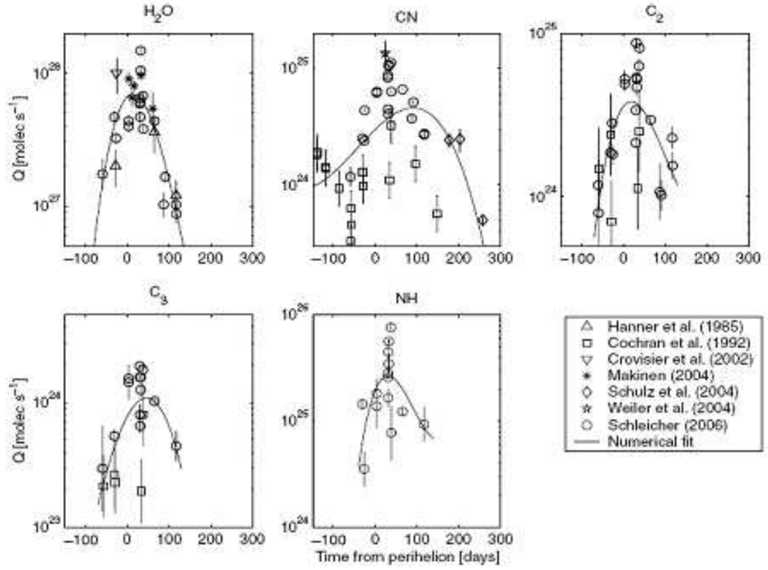

Figure 3.9: Observed gas production rates versus time from perihelion for Comet 67P/Churyumov–Gerasimenko [9].

of least squares, which leads to the following equation:

$$\log_{10}(Q_x) = \sum_{i=0}^{3} a_i \left(\frac{T - b_1}{b_2}\right)^i$$

Where Q_x is the speed of production of the gas species X expressed in molecules/sec, T is the number of days from perihelion (which is a positive value if it refers to the post-perihelion period), and a and b are species-specific coefficients.

If"T" falls outside the range of validity, a simplified formula can be used (but only as a first approximation):

$$Q_x = A_j r_h^{-B_j}$$

Where A and B are species-specific and also perihelion period-specific coefficients, meaning that their value depend also on the considered perihelion period (pre- or post-perihelion).

3.2.10 Dust production

Dust is one of the main elements presents in the emissions from the cometary surface. Attaining an adequate level of exposure to dusts is of decisive importance for the achievement of some goals of Rosetta mission; however, the impact or the deposit of dust on some sensitive surfaces of the satellite may be dangerous for its activity and may thereby cause a failure of the mission. When previous investigative missions, such as Giotto and Deep Impact, made their close approach to the comets, the space probes were hit by large size dust particles, mainly in the order of a few millimeters, which damaged some of their scientific sensors and caused a relevant deviation from their desired attitude. However the approach speed of Giotto and Deep Impact was much higher (in the order of Km/s) than that expected for Rosetta (a few m/s).
It is therefore necessary to have a model of the foliage of 67P/CG order to predict the flow and the speed of the powders inside a function of time and space. Through a study of the flow of the powders is also possible to have an estimation of the level of light radiation on the surface, so going to check the operating conditions of the solar panels of the lander Philae.
Several authors have addressed this problem [12] [13] by recovering the parameters required by astronomical observations or using those of other comets, such as those measured in-situ for comet Halley explored by Giotto in 1986 (such as the mass distribution). From the data of similar comets it can be seen that water and CO are the main elements of the gases, while the powder particles are formed by silicates and carbonaceous materials with a size ranging from a few nanometers to millimeters.
To go back to the production of powder of a comet were used the parameter $Af\rho$ that is obtained by photometric observations and defined as the product of the albedo (the reflectivity of the grain), fill factor (related to the optical density of the foliage, it describes how much occupies the canopy than the field of view) and ρ (radius of the crown). The parameter $Af\rho$ is related to speed of production $Q_{d,j}$ relative of to the particle size S_j with the emission rate $v_{d,j}$, to the value of albedo geometric p and the phase function $j(\alpha)$,

according to the relation:

$$Af\rho = 2\pi p j(\alpha) \sum_j s_j^2 \frac{Q_{d,j}}{v_{d,j}}$$

The albedo geometric p and the phase function $j(\alpha)$ link the cross-section of a particle of dust with the light diffused by it. The phase angle α is the angle between the direction of the observer and that of the incident radiation, viewed from the particle that spreads. The geometric albedo of an object is defined as the ratio of the intensity reflected back from the object, $\alpha = 0$, and the total intensity diffused. The phase function $j(\alpha)$ provides the ratio of the intensity diffused in the direction α respect to the intensity diffused to $\alpha = 0$. For the 67P/CG is considered the function of geometric phase represented in Figure 3.10 , assuming a geometry emission axial-symmetric with peak activity in the subsolar point. This hypothesis is required and the reason is that if an observer looks in the direction perpendicular to the direction of emission of the particle, this will tend to leave the field of view very quickly than when you look in a parallel direction. Hence the number of particles inside the field of view (which may dramatically influence the value of $Af\rho$ measured) depends on the angle between the direction of emission of the particles and the direction of the observer.

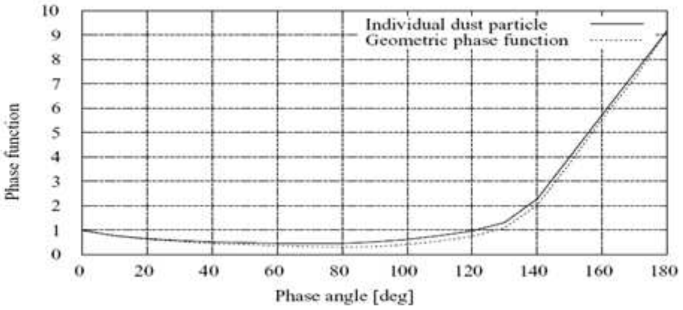

Figure 3.10: *Solid line*: phase function of an individual dust particle as given in Divine (1981), but here normalised to $j(\alpha = 0) = 1$. *Dashed line*: geometric phase function $j_{geo}(\alpha)$ Müller (1999) [13].

The values of $Af\rho$ measured for 67P/CG were recorded during its approach to perihelion of 1982/1983, 1996/1997 and 2002/2003 by several authors (Storrs 1992; Osip 1992; A 'Hearn 1995; Kidger 2003; Lamy 2003; Weiler 2004; Schulz 2004; Feldman 2004; Schleicher 2006) and the results are shown in Figure 3.11 as a function of days at perihelion. By adopting the correction phase angle for the geometric phase function were obtained values for $Af\rho$

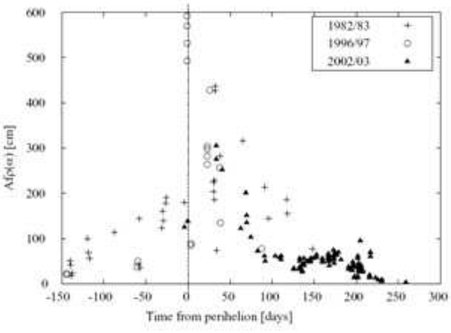

Figure 3.11: Observed $Af\rho$ values as function of heliocentric distance r_h [13].

as shown in Figure 3.12, together with a law:

$$Af\rho(r_h, \alpha = 0) = 2393\left|\frac{r_h}{1AU}\right|^{-5.08}$$

that represents the interpolation points found, where $Af\rho$ is expressed in [cm] r_h is the distance from the sun in astronomical units.

In Figure 3.13, is instead represented the speed of production of H_2O

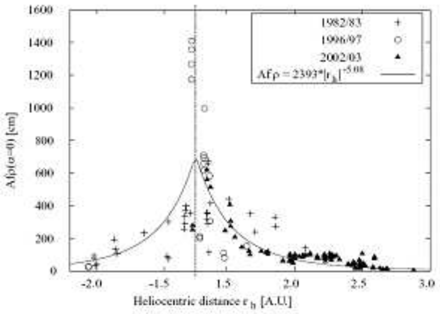

Figure 3.12: Observed $Af\rho$ values corrected for phase angle through division by the geometric phase function and power law fit for phase-angle-corrected [13].

observed (Hanner 1985, Feldman 2004, Makinen 2004, Crovisier 2002)[9], together with the law of interpolation curve:

$$Q_{H_2O}[mol/sec] = 3.4e^{28}|r_h|^{-5.71}$$

Both the index $Af\rho$ and the production of H_2O show their maximum approximately 30 days after the perihelion passage, while a second peak of production of powders occurs after about 200 days at a distance of about

2.5 AU. Soon after, between 2.5 and 3 AU may be noted a sharp decline in production of dust, and beyond 3 AU all the checks show a pointed nucleus [14].

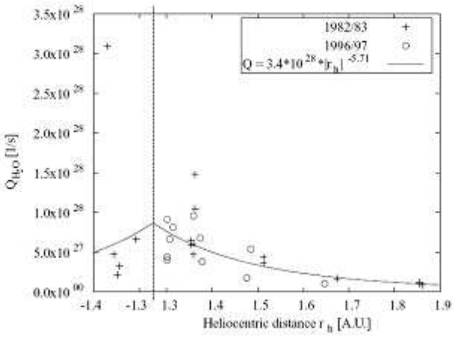

Figure 3.13: Measured H_2O production rates with corresponding power law [13].

3.2.11 Dynamics of comet dust

A comet is an agglomeration of ice and dust. When the comet reaches the distance of about 3 AU, the ice near the surface begins to sublimate releasing the dust trapped in it. Inside the canopy, within a few rays from the surface of the nucleus, the motion of the powder grains is coupled with the flow of gases emitted from the nucleus and are accelerated; over ten times the radius of the core expanding gas becomes too diluted to exert an appropriate force and the flow of powder is decoupled from that of the gas; in this zone the particles have reached their maximum speed, said final speed, which is proportional to $\frac{1}{\sqrt{\rho s}}$ where ρ is the density of the particle of radius s, and is used to interface the part of the crown in which case the acceleration of the particles, dominated by the forces of emission and the severity of the nucleus of the comet, with the part where the dynamics is governed by radiation pressure and the severity of the Sun.

In addition to the canopy, the powders form the typical tail direct in the opposite direction to the Sun, because of the pressure of radiation, within which the position of the particle is a function of the pressure coefficient of β radiation and the emission time. The coefficient β takes into account the radiation pressure and the gravity of the Sun, and it is defined as:

$$\beta = \frac{3L_{\odot}}{16\pi c G M_{\odot}} \frac{Q_{pr}}{\rho s}$$

Where $L_\odot$ and $M_\odot$ are the luminosity and the mass of the Sun, c is the speed of light, G is the gravitational constant and q_{pr} is the efficiency of the radiation pressure, that represents the properties of absorption and scattering of grain averaged over the entire solar spectrum and depends on the material.
In order to understand the formation of dust tails, the concepts of synchrones and syndynes were introduced by Bredikhin (1903). Synchrones are the positions of particles of different β emitted at a given time, while syndynes describe the positions of particles of fixed β and varying emission time. Both terms refer to hypothetical particles emitted with zero velocity relative to the nucleus. Since, realistically, the initial velocity of a dust grain is different from zero, the resulting synchrone or syndyne will have a finite cross section with a radius proportional to the product of dust emission speed and time elapsed since emission. In particular, grains released at a given time with isotropic speed will form a spherical shell the centre of which moves along the appropriate syndyne.

While for particle sizes on the order of the dominant wavelengths of the solar spectrum (0.01 ... $1\mu m$) β depends sensitively on material, shape, structure and size of the particles (Burns et al., 1979), it is about constant for much smaller particles and proportional to $\frac{1}{\rho s}$ for large ones, i.e. in the geometric optics regime (Gustafson, 1994) [13].

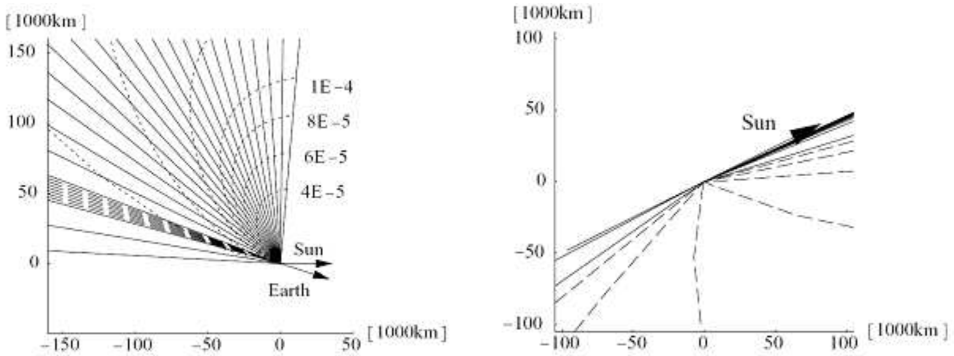

Figure 3.14: Synchrones are shown projected in the comet orbit plane (*left*) and image plane (*right*). The *solid* lines correspond to synchrones for different period of times, the *dashed* lines correspond to syndynes for different values of β [13].

In the literature, both the exponents γ of the cumulative mass distribution $F(m) \sim m - \gamma$ and α of the differential size distribution $g(s) \sim s\alpha$ are commonly used. If a constant particle bulk density is assumed in the concerned interval, the exponents γ and α are related as $\alpha = -3\gamma - 1$.
In Table 3.6 are shown the exponents determined by several authors through

the use of photometric observations of the comet 67P/CG and by in-situ measurements of other comets (Halley 1986), while the Figure shows the chart who sets the trend of the percentage of particles as a function of size.
Agarwal proposed different mathematical models which allow to reproduce

Table 3.6: Values of α and γ found in the literature.

	α	γ
Divine and Newburn	-4.3	1.1
Agarwal	-3.7	0.9
Fulle	-3.3	0.8

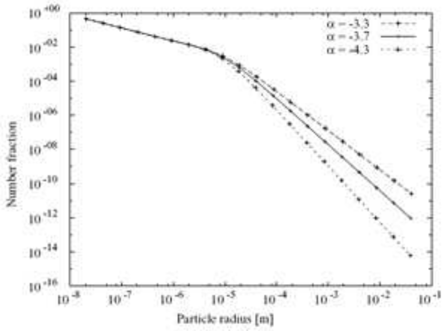

Figure 3.15: Number fraction over particle radius for the three differential size distributions [13].

the evolution of the canopy and the mass flow emitted. The first simplified model is defined as a model radialsymmetric in which the activity of the surface is uniformly distributed on the surface of the comet; the second is a model based on insulation (Insulation driven), for which the surface is homogeneous and issuing activity is proportional to the amount of radiation received; finally the model jets, in which the activity on the surface of the comet is described by a Gaussian centred in the subsolar point.
Additionally, for all models is considered a core of spherical shape of radius 2 Km in which the grains of powder are divided into classes depending on the mass, and is also considered to be a constant density for grains of 1000 Kg/m^3. In a first step is calculated by the flow of gas, at which the powder is coupled at least in the instants immediately after issuance from the nucleus; thereafter the trajectories of the grains are integrated considering the severity of the core and the resistance force exerted by the gas. For simplicity gases are considered H_2O and CO, whose production speed are used

as input to the model, together with the values of $Af\rho$, the phase function, mass distribution and final velocities determined.

3.2.12 Optical opacity due to dust

A study of optical opacity due to dust has been carried out in accordance with the standard Insulation driven and jets [13]. The optical opacity (Optical Depth, τ) is a measure of transparency and expresses the amount of light removed from a radius by diffusion or absorption. If I_0 is the intensity of light at the source, and I is the intensity of light observed after a certain path, τ is defined by the following expression:

$$\frac{I}{I_0} = e^{-\tau}$$

The optical opacity in the case of a comet is influenced by the parameters $Af\rho$, phase function, albedo of dust and efficiency of extinction. The first three parameters are easily obtained through observations from Earth, while for the last estimate is a value between 1 and 2. For the optical opacity has been identified, for the worst conditions, a maximum value of 0.2, taking into account the line of sight to the Sun-surface of the nucleus in the subsolar point at perihelion, considering the model jet, then the most burdensome. Since the optical opacity is proportional to the value of $Af\rho$, by the law of interpolation, has determined a value of τ for all the way from the comet at 3 AU until perihelion as shown in the Figure 3.16, while in the Figure 3.17 is shown the trend light intensity as a function of distance from the Sun considering the optical opacity calculated.

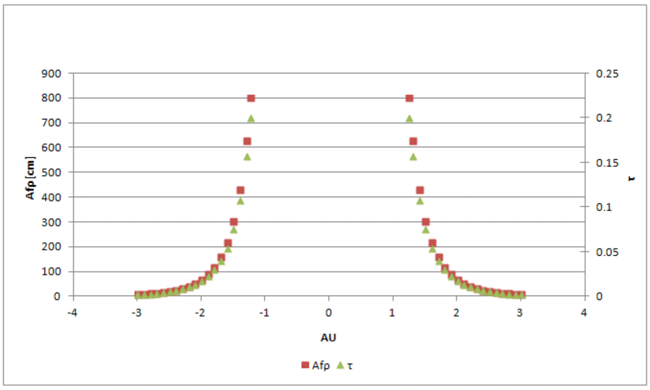

Figure 3.16: Trend of the value of $Af\tau$ and τ as a function of distance from the Sun [1]

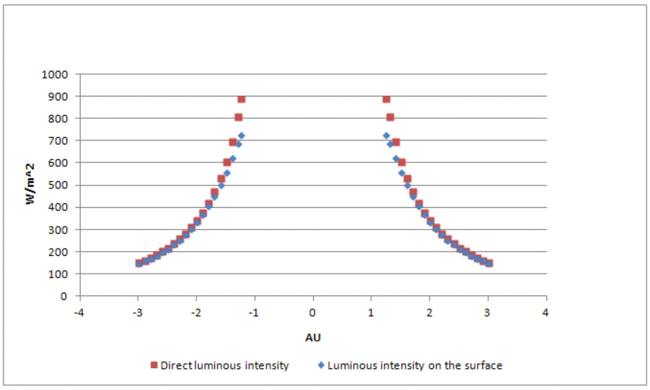

Figure 3.17: Performance of the light intensity with and without τ as a function of distance from the Sun [1].

3.2.13 Lighting conditions

At this point it is possible to make some reasonable assumptions and calculate the variation of the light radiation on the surface of the comet 67P/CG a function of time. Considering only the period of the mission of the lander Philae (counting the day of landing), 10 November 2014, as the first day or as -276 day before the perihelion of the comet that will be at 13 August 2015. Shall be adopted various hypotheses derived from the discussions in the preceding paragraphs, including the inclination axis, which is directed toward the north right ascension of 40° and declination of 70°. The period is assumed, as mentioned earlier, of a duration of 12.68 hours. Also for simplicity is assumed a spherical shape for the nucleus of the comet. With the choice made on the axis will be had the spring equinox (here corresponds to a aerocentric longitude at 0°) on 13 March 2015 (which correspond to the 123 days of the mission of the lander) and the autumnal equinox on 26 December 2015. The value of optical opacity τ assumes variable and follows the trend described in the previous section, while in the first approximation the contribution of the scattered light is considered negligible. A solar panel on the surface of the comet will then receive a light radiation equal to:

$$I(r, \tau, \delta, \phi, d\phi, w, dw) = \\ i(r)^{-\tau m_z} \sin(\phi + d\phi)\sin(\delta) + \cos(\phi + d\phi)\cos(\delta)\cos(w + dw)$$

Where $I(r)$ is the total light radiation at a distance r of the comet from the Sun, m_z is the air mass (in this case we consider the comet's coma as an atmosphere), ϕ is the latitude and $d\phi$ is the tilt angle of the solar panel to the north, δ is the declination of the Sun, then w is the hour angle of the Sun ($= 0$ at noon) and dw is the inclination of the panel towards the east.

Whereas a horizontal panel relative to the surface of the comet. Considering the landing equator we can calculate the radiation intensity during the hours of the day, for example for the first 10 days of mission is obtained the graph of Figure 3.19. In addition, by calculating the vector Sun, always starting from the equator landing day until the day of perihelion, is obtained the graph of Figure 3.20.

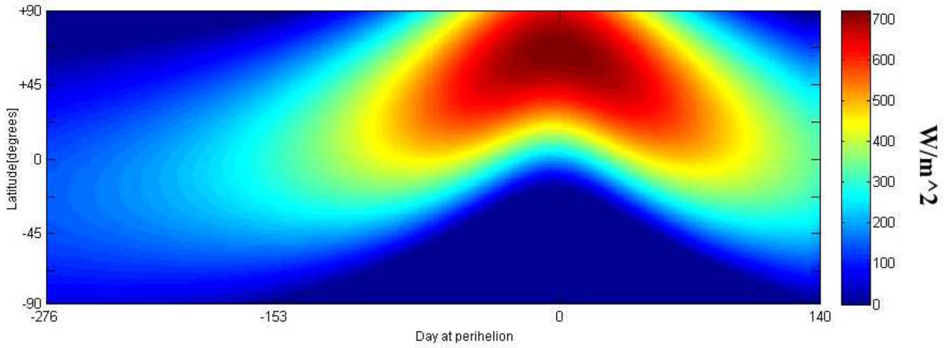

Figure 3.18: Light intensity of the soil of the comet as a function of the days at perihelion. Are indicated respectively, the day of the lander landing, the spring equinox, the perihelion and the nominal end of mission, 31/12/2015 [1].

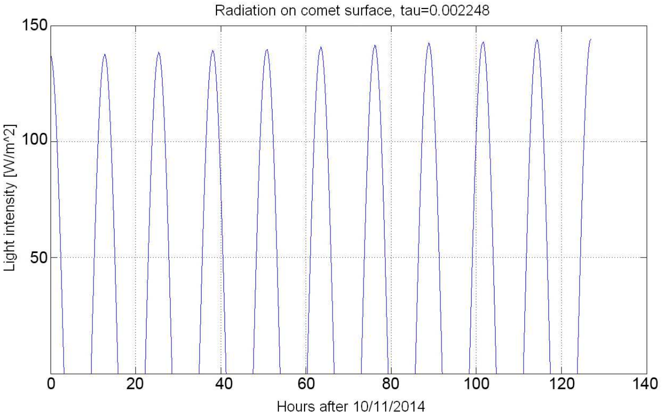

Figure 3.19: Light intensity on a horizontal panel during the first 10-day mission at the equator [1].

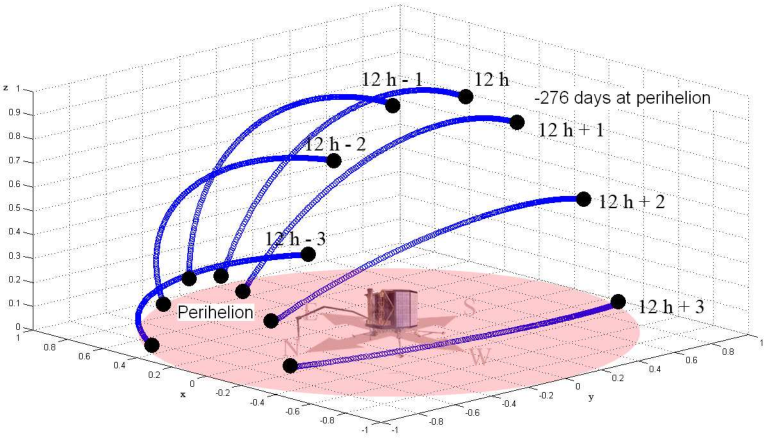

Figure 3.20: Vector Sun at intervals of one hour for a landing probe on the equator, from the first day of the mission to the comet's perihelion [1].

3.3 The spacecraft

A brief description of the spacecraft is presented in various reports [3] [4]. The total mass at launch was about 2900 kg, divided between 1720 kg of propellant, 165 kg of scientific payload and 100 kg of Philae. Rosetta spacecraft is 3-axis stabilized and its core is constituted by a $2.8 \times 2.1 \times 2.0$ m aluminium box. On the top of this box the Payload Support Module is located where all scientific instruments are mounted. On the other hand the subsystems are placed on the base, in the Bus Support Module. For power production two opposed extended appendages carry the solar panels constituted by dedicate-developed Low Intensity Low Temperature solar cells. Each solar panel is 14 m long and displaying 30 m^2 surface. Power production capabilities are 850 W at 3.4 AU up to 8700 W close to perihelion. Solar panel wings can rotate of $\pm 180°$ on the appendage axis for Sun exposure optimization.
Earth communication is guaranteed through a 2.2 m steerable high gain antenna attached at the back panel, while in the front panel Philae is stowed and will communicate with the orbiter through a medium gain antenna.
Rosetta orbiter attitude during close comet observation is designed to have the instruments pointing towards the comet, while the antenna and solar panels are pointed towards Earth and Sun respectively.
Thermal control in the hot case is ensured through thermal radiators and louvers located in the back of the spacecraft, while in the cold case through heaters. Insolation is guaranteed through Multi-layer insulation (MLI) blankets.

For propulsion 10 bi-propellant thrusters of 24 N are used, and can be also exploited for attitude control. [16]
The scientific instruments on board of the Rosetta orbiter are [3]:

- **ALICE** An ultraviolet imaging spectrograph (Alan Stern, SRI, Boulder (USA))

- **OSIRIS** Optical, Spectroscopic, and Infrared Remote Imaging System (Horst-Uwe Keller, MPS, Lindau (D))

- **VIRTIS** Visible and Infrared Thermal Imaging Spectrometer (Angioletta Coradini, IAS-CNR, Rome, (I))

- **MIRO** Microwave Instrument for the Rosetta Orbiter (Sam Gulkis, JPL, Pasadena, (USA))

- **CONSERT** Comet Nucleus Sounding Experiment by Radiowave Transmission (Wlodek Kofman, LPG, CNRS/UJF, Grenoble (F))

- **ROSINA** Rosetta Orbiter Spectrometer for Ion and Neutral Analysis (Hans Balsiger, Universität Bern (CH)

- **MIDAS** Micro-Imaging Dust Analysis System (Willi Riedler, IWF, Graz, (A))

- **COSIMA** Cometary Secondary Ion Mass Analyzer (Martin Hilchenbach (formerly Jochen Kissel), MPS, Lindau (D))

- **GIADA** Grain Impact Analyzer and Dust Accumulator (Luigi Colangelo, INAF, Naples (I))

- **RPC** Rosetta Plasma Consortium (Anders Eriksson (formerly Rolf Bostrom), IRF Uppsala IRF Uppsala, (S), Jim Burch, SRI, San Antonio, (USA), Karl-Heinz Glassmeier, IGEP, Braunschweig, (D), Rickard Lundin, IRF, Kiruna (S), Jean-Gabriele Trotignon, LPCE/CNRS, Orleans (F), Chris Carr, Imperial College, London (ENG))

- **RSI** Radio Science Investigation (Martin Patzold, Universitat Koln (D))

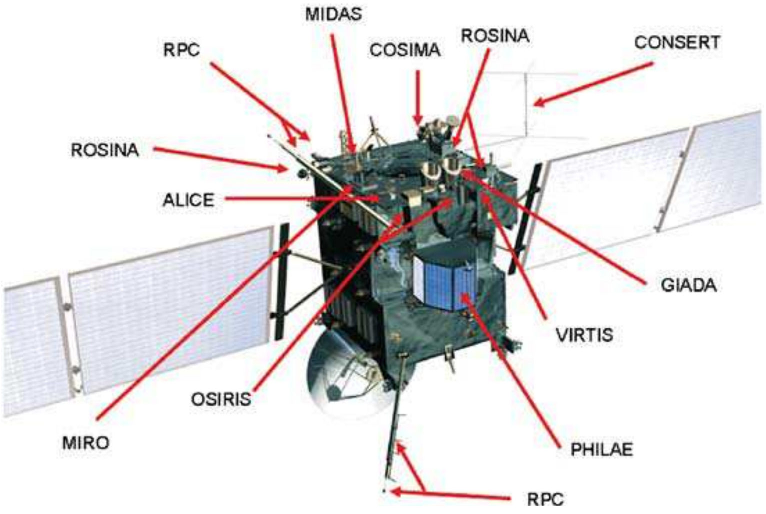

Figure 3.21: The Rosetta spacecraft and its scientific payload [3].

3.4 The lander Philae

The lander Philae will investigate the comet 67P/CG in-situ, while the space probe Rosetta will operate from orbit. The Lander system has been provided by an international consortium (Germany (lead), France, Italy, Hungary, Finland, UK, Ireland and Austria) and supports a scientific payload of 10 instruments [39]. It is operated by the Lander Control Center (LCC) at DLR, Cologne, and the Science Operation and Navigation Center (SONC) at CNES, Toulouse, via the European Spacecraft Operations Center (ESOC) in Darmstadt. Since the launch the lander has been operational during commissioning, by performing several checkout as well as some activities for calibration and failure investigation. The location of Philae in the Rosetta configuration is visible in 3.21.

All the manoeuvres during flight are performed by Rosetta, while Philae is prepared to the descent and on-comet operations. The lander entered in the hibernation phase together with the space probe pending to reach the target comet. However separation, descent and landing strategy are not yet fully outlined as there's the necessity to characterize first the comet nucleus from orbit, where shape, state of rotation, gravitational field as well as gas and dust environment are relevant key parameters.

The deployed configuration of the Lander is visible in Figure 3.22. The lander is designed to detach itself from the main spacecraft and fall towards the comet along a ballistic trajectory (see Figure 3.23). To reduce the chance of bouncing during initial impact the legs are designed to damp during the landing, and to avoid possible detachment from the comet surface it will harpoon itself to it. Eventually is possible to activate a motor on the Lid to obtain a tighter anchoring to the comet nucleus. The lander main operative phases are Separation, Descent, and Landing (SDL), First Science Sequence (FSS) and Long Term Science (LTS). The first two phases last for 5 comet days (i.e. about 60 hours) after the separation from Rosetta space probe and

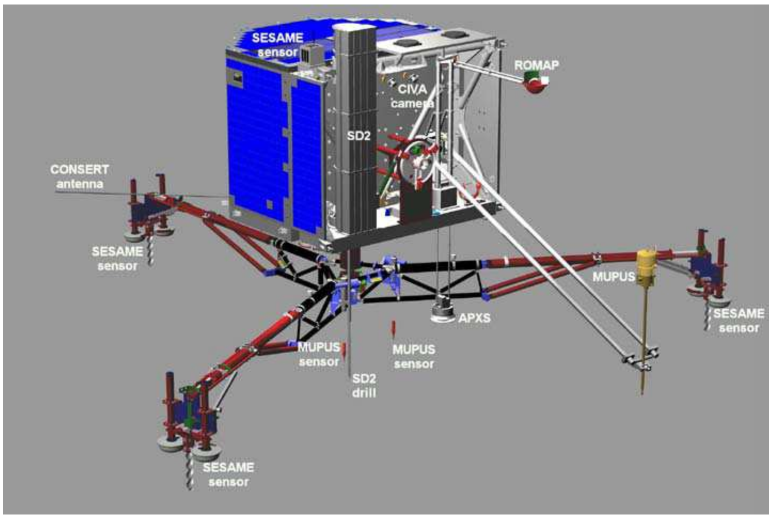

Figure 3.22: Rosetta Lander, Philae, in landed configuration [32].

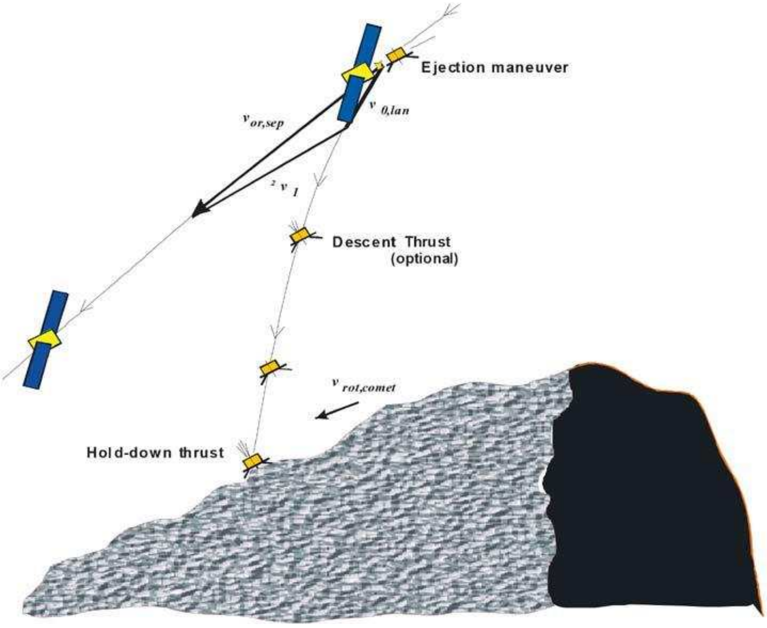

Figure 3.23: Philae landing scenario [30].

the power demand is satisfied by the primary battery. The LTS instead will last depending on the success of the Solar Array System (SAS) to produce power [32]. The total mass is about 100 kg, and most of the surface is covered with solar cells, with the objective of extending LTS by providing additional power to the PSS (Power SubSystem) to charge the secondary battery.
The scientific objectives of the Lander are the determination of the composition of cometary surface matter, including the possible presence of organic materials, as well as the investigation of the structure and physical, chemical and mineralogical properties of a comet's surface, including the local depth structure (stratigraphy) and global internal structure of a comet's nucleus. Communication with Earth of all the data and the telemetry will be through the high gain antenna on Rosetta space probe, which will function as communication bridge. [17]
The Rosetta lander scientific instruments are [3]

- **APX** Alpha Proton X-ray Spectrometer (G. Klingelhofer/R.Rieder; University of Mainz/ Max Planck Inst. (D))
- **COSAC** The COmetary SAmpling and Composition (F. Goesmann, H. Rosenbauer; MPS, Max Planck Inst. (D))
- **Ptolemy** Evolved Gas Analyzer (I.Wright, C.Pillinger, J.Zarnecki; Open University (UK))
- **CIVA** Comet Nucleus Infrared and Visible Analyzer (J.P.Bibring; IAS (F))
- **ROLIS** Rosetta Lander Imaging System (S.Mottola; DLR (D))
- **CONSERT** COmet Nucleus Sounding Experiment by Radiowave Transmission (W.Kofman; LPG (F))
- **MUPUS** MUlti-PUrpose Sensors for Surface and Sub-Surface Science (T.Spohn; University of Munster (D))
- **ROMAP** Rosetta Lander Magnetometer and Plasma Monitor (U.Auster, I.Apathy; Max Planck I. extraterr. Physics, TU Braunschweig(D)/ KFKI (H))
- **SESAME** Surface Electric Sounding and Acoustic Monitoring Experiment (K.Seidensticker, D.Mohlmann, W.Schmidt, I.Apathy; DLR (D)/ FMI (SF)/ KFKI (H))
- **SD2** The sampling, drilling and distribution subsystem (A.Ercoli-Finzi; Politecnico di Milano (I))

3.4.1 Philae design

Philae main body shape is a trapezoidal box, constituted of carbon fibre and carbon fibre with aluminium honeycomb. It consists of a ground plate, an experiment platform and a polygonal sandwich construction, the Solar Hood, covering the Warm Compartment and carrying the solar generator. On the external faces (named WALLs) the 6 LILT solar arrays are mounted and constitute the Solar Hood [4]. The produced power is stored in the secondary batteries, although Philae is provided also with primary non rechargeable batteries useful for the First Science Sequence (this aspect is treated extensively in subsection 3.4.2). Only one face of the box is open, the Balcony, and it serves as payload support and external interface. The main body core is called Warm Compartment which is thermally insulated with respect to the external environment through an MLI blanket and contains all the vital subsystems of the spacecraft.

Philae main body is supported on a tripodal landing gear, each of the three foot is provided with integrated sensors and ice screws. The latter are necessary to guarantee stability and firmness on the cometary soil. Philae is also provided with a harpoon, deployable through a 2.5 m tether which is designed to grab, hold and fix the lander to the comet soil during the landing manoeuvre.

Philae mechanical capabilities permit to the lander to rotate of 360° around its z axis, this solution permits to define a “working circle” for collection of samples, deployment of instruments and orientation of the solar arrays. Philae has also a small tilting capability of about ±5°.

Philae attitude during the Separation Descending landing manoeuvre is guaranteed through a flywheel and also through cold gas impulsive chemical thrusters.

Communication of Philae with Rosetta is performed through a series of s-band antennas placed on the external body of the lander, antennas switch on periodically using a mechanical device. [16]

3.4.2 Philae Power SubSystem

The Power SubSystem (PSS) is the system demanded to manage the power generation, control and distribution on the lander.

During the cruise phase, when Philae is attached to the Orbiter, all the systems are powered via ESS (Electrical Support System) by the Rosetta power system. Remarkable is that the Rosetta mission is the first deep space mission that will go beyond the main asteroid belt relying only on solar cells for power generation [40].

As Philae is detached, power provision is given by a Battery unit, consisting of a Primary and Secondary unit, and the Solar Array (SA) Generator. The main source of power is represented by the lander Primary Battery, with capacity of 1200 Wh (1000 Wh at comet arrival) capable of feeding the lander up to 5 days to assure the minimum scientific research required by the mission profile, with a support of a Secondary Battery, initial and on comet capacity of 150 Wh and 130 Wh respectively. The Secondary Battery is rechargeable through Solar Arrays.

This configuration is adopted to make it possible the execution of Long Term Science (LTS), so maximizing the scientific return of the mission by extending the operational life of Philae: as the comet approaches the perihelion of the orbit the solar radiation increases. Power distribution is basically performed via the Lander Primary Bus (non-stabilized, +28 V baseline) [40].

During the comet in-situ investigations there is power production thanks to the 1.4 m^2 Solar Arrays which will produce about 8 W . This result is achieved thanks to new LILT solar cells capable to generate energy in the very tough environment in which Rosetta and Philae will have to survive and work.

The architecture chosen for the electrical system is the Maximum Power Point Tracker system: it places Maximum Power Point Trackers (MPPT) between the solar panels and the loads.

Solar cells have complex relationship between solar irradiation, temperature and total resistance that produces a non-linear output efficiency, know as the I-V curve: the use of the MPPT is to obtain the maximum power out of a solar panel by sampling the output of the cells and applying the proper resistance.

While the MPPT conversion efficiency from the solar cell output to the lander bus is relatively high (around 95% or higher) the major loss derives by the scanning along the I-V curve to reach the maximum power point, where the loss is generally higher, up to 25% [17].

3.4.3 Solar arrays design

The Philae's solar arrays was projected to be utilized at the atmospheric condition of the comet 67P/CG, this means low temperature around -160°C and at the solar distance of 3 AU. For this reason LILT solar cells have been used.

The Solar cells are mounted on the surfaces of the Solar hood, which covers the Lander internal compartment. Following the surface orientation, each array is orientated towards another direction, to enable the Lander to generate power whenever possible without solar hood movements to follow the

Sun. Only the Lander "balcony" (Lander X-direction) is not covered with Solar cells. Due to the Solar hood partitioning, the solar generator consists of 8 panels, which are grouped in 6 electrical sections. Two panels (Balcony 1 and Balcony 2) are prolonging the solar hood panels Wall 1 respectively Wall 5 until the end of the Lander balcony (see Figure 3.24).

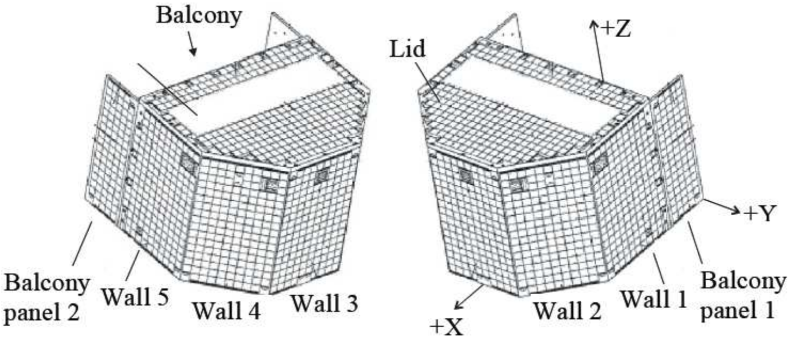

Figure 3.24: Philae solar array [29].

The solar array are connected to MPPT to adapt the generated voltages and currents to the Lander Primary Bus requirements. Since Wall 1/Balcony 1 and Wall 5/Balcony 2 are facing opposite direction on the Solar hood, and thus never will be illuminated at the same time, both outputs are connected to the same MPPT.

The electric component of the Philae solar array is composed of 1224 solar cells of the same dimension 33.7 × 32.4 mm^2 and 200 μm of thickness. Table 3.7 shows the division of cells in the panels.

Table 3.7: Number of strings and cells per module

Electric section	Strings in panel (p)	Cells in string (s)	Array dimension $[m^2]$ (active cell area)
LID	2	115	0.25113
Wall 1 and Balcony 1	2	127	0.27734
Wall 2	2	81	0.17688
Wall 3	2	81	0.17688
Wall 4	2	81	0.17688
Wall 5 and Balcony 2	2	127	0.27734
total solar cells		1224	1.33645

3.4.4 General description of the solar cells

The solar cells are silicon of the type 10LiTHI-ETA®3ID/200, them were developed by RWE in the years 1990-96 [29]. The main characteristic of the cell are:

- 10 ohm cm CZ base material.
- N+/pp+ structure.
- Front and rear side oxide passivation.
- All rear side reflector.
- Photolitography defined grid lines.
- Heavy n++ diffusion under the front contact grid and p+ guard ring channel-stopper around the edges of the cell.
- Shallow, radiation resistant emitter.
- Back surface field with local p+.
- Non reflective front surface by inverted pyramids.
- Coverglass: CMX Pilkington 100 μm thickness, not conducting.
- Blocking diodes: Microsemi JANS 1N5811 (1 per string, 12 in total since there are 12 strings; there is another diode after each MPPT).
- Wiring: generally with AWG 24 (cross section 0.2047 mm^2).
- Cement for cover-glassing/lay-down: Siliconic resin RTV-S695/RTV-S691.

N.B.: It is not clear whether the PHILAE solar cell coverglass is antireflection (AR) coated. The documentation is contradictory.
The conservative approach is to consider the glassed solar cells as not being AR-coated. [29]
The n+ emitter and the p+ channel-stopper form a diode n+/p+, which in reverse bias works as an integrated by-pass diode with a reversible Zener break-through voltage of 6-8 V.

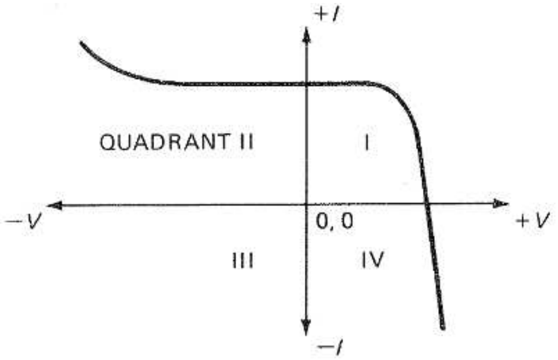

Figure 3.25: Conventional solar cell I-V curve in 3 quadrants. In quadrant I, power is produced; in quadrant II, the cell is reverse-biased [29].

3.4.5 Output power

The precise prediction of the output power of Philae's solar generator is an important requirement for successful planning of the LTS phase. The usable output power and its integral, output energy, depends on a multitude of parameters (listed below) and will be affected with a degree of uncertainty depending on the complexity of models and measured data used.
The usable output power of the Philae solar generator depends on:

- Solar array cell constants (BOL, EOL, temperature dependence).
- Areas and normal vectors of panels/strings.
- String parameters (diode drop, harness/connector resistance, cell mismatch losses).
- Solar constant and heliocentric distance: direct beam irradiation at the Lander location (and coma dust optical depth).
- Comet albedo (for scattered light if significant): indirect irradiation at the Lander location.
- Incidence angle between panel normal and sun direction .
- Temperature of solar cell (from complete Thermal Mathematical Model or approximate models) function of (direct and indirect) solar irradiation and temperature of comet surface with the Lander horizon.
- Cumulated equivalent radiation fluences at time of Lander mission.
- "Remaining factors" (degradation factors apart from radiation damage).

- Dust model (if dust/ice degradation is assumed).
- MPPT model (efficiency or dissipation as function of input power, voltage, current, temperature, . . .).
- Shadowing (fraction of each cell of a particular string shadowed).

3.4.6 Variation due to Solar Constant

Given a certain solar constant S, the electrical parameters of the I-V curve are calculated through

$$\begin{aligned}
I_{SC} &= \frac{S}{S_{ref}} I_{SC,ref} \\
V_{OC} &= V_{OC,ref} + \left(1 - \frac{S}{S_{ref}}\right) I_{SC,ref} R_S + \frac{aKT}{q} \ln\left(\frac{S}{S_{ref}}\right) \\
I_{mp} &= V_{mp,ref} - \left(1 - \frac{S}{S_{ref}}\right) I_{SC,ref} \\
V_{mp} &= V_{mp,ref} + \left(1 - \frac{S}{S_{ref}}\right) I_{SC,ref} R_S + \frac{aKT}{q} \ln\left(\frac{S}{S_{ref}}\right)
\end{aligned}$$

where the subscript “ref” indicates the reference values measured at S_{ref} (R_S, a, K, and T are constants).

3.4.7 Degradation due to Radiation

Once the characteristic parameters of the I-V curve have been calculated in BOL condition, their propagation to EOL condition can be done with

$$X_{EOL,SC}(T_{ref}) = X_{BOL,SC}(T_r ef) RF_x$$

where X is the generic parameter (i.e., $I_s c$, $V_o c$, $I_m p$, $V_m p$), $T_r ef$ is the reference temperature, and RF_x is the remaining factor of the parameter X, $T_r ef$ is the reference temperature at which the parameters are measured. If X has to be computed at a different temperature, the variation of the temperature coefficients with the fluence has to be considered. Nevertheless, this relation is non trivial and, in first approximation, the temperature coefficients are considered not to vary with the radiation.

3.4.8 Variation due to temperature

The temperature effect on the parameter X is taken into account through

$$X_{EOL,SC}(T) = X_{EOL,SC}(T_{ref}) - \beta_{EOL,SC}(T_{ref} - T) \tag{3.1}$$

$$\beta_{EOL,SC} = \frac{\partial X}{\partial T}_{EOL,SC} \tag{3.2}$$

where β is the temperature coefficient. In Equation 3.1 the temperature coefficient has to be computed in EOL condition.
Note also that the linear variation of parameters with temperature is an approximation applicable over finite temperature ranges. Generally, the parameters can be expressed as polynomials in T (up to 5th order for extreme temperature ranges -160°C to +160°C).

3.4.9 Variation with incidence angle

The ideal response of solar cells to the incidence angle follows the cosine. However, due to Fresnel reflection and multiple reflections in the system AR-coating, glass, adhesive, cell the real factor (called "Kelley cosine" in the engineering literature) is a function that drops to zero faster than the cosine and is zero for $\theta > 85°$: Beyond 50°, the electrical output deviates significantly from the cosine law, and the cell generates no power beyond 85°, although the mathematical cosine law predicts 7.5% power production.

Table 3.8: The Kelly cosine values of the photocurrent in silicon cells [23]

Incidence angle [°]	Mathematical cosine value	Kelly cosine value
30	0.866	0.866
50	0.643	0.635
60	0.500	0.450
80	0.174	0.100
85	0.087	0

Chapter 4

Design of the experimental apparatus for LILT measurements

The I–V characteristics (or I–V curve) of a photovoltaic cell, module or array is the important key for identifying its quality and performance as a function of varying environmental parameters, such as solar radiation and ambient temperature. The curve indicates the characteristic parameters of the photovoltaic generator represented in short circuit current, open circuit voltage and the point of maximum power at which the generator would work at its peak efficiency [38]. For this reason it is realized an experimental apparatus that cools down the solar cell under illumination, measure the I-V curve and send all the data of current and voltage to a computer environment.

4.1 Base plate and cooling coil

The first component realized is the cooling coil. The aim of this piece is to cool the temperature of the solar cell with the aid of liquid nitrogen. The dimensions of the cooling coil are $80 \times 70 \times 18$ mm and the material is copper, that is one of the best thermal conductive material.
The component is composed of two pieces, which are hold together trough 15 screws. In the first piece (see Figure 4.1) there is only the incision of the half coil and the holes for the screws. The second pieces (Figure 4.2) is identical to the first, with in addition an incision on the top for putting the cell and the cables.
In the first hole of the coil there is the screw thread for the connection of the liquid nitrogen tube, while the nitrogen coming out from the second hole is in largely gas.

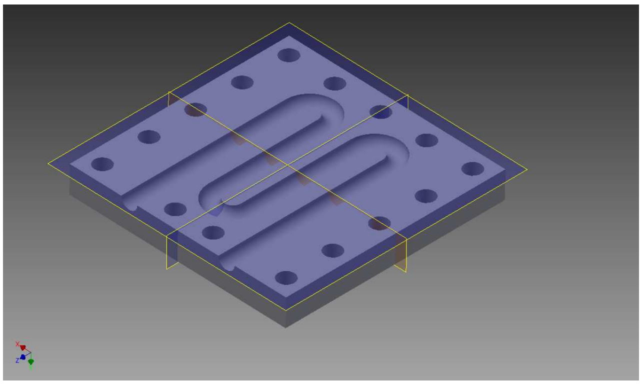

Figure 4.1: Internal vista of half (coil made with Autodesk Inventor).

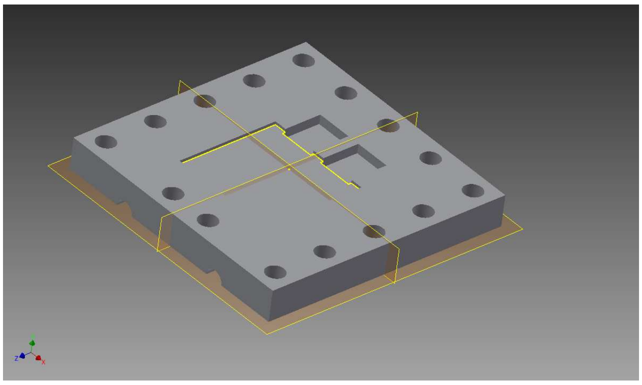

Figure 4.2: External vista of half coil (made with Autodesk Inventor).

In Figure 4.3 it is possible to see the final cooling coil with the connection for the nitrogen liquid pipe.
Before building the definitive cooling coil it was build one in aluminium. With this prototype we have made the first test with the liquid nitrogen and it was possible to note the following problems:

- To establish the temperature of the solar cell is fundamental to insert a thermocouple under the solar cell.

- Between the coil and the solar cell it is necessary to put a thermal filler, to be sure that the cell adheres at the coil, and that the measure of the thermocouple is correct.

- The positive pole of the solar cell must not be in contact with the copper, for this reason the solar cell is isolated with an electric isolating tape.

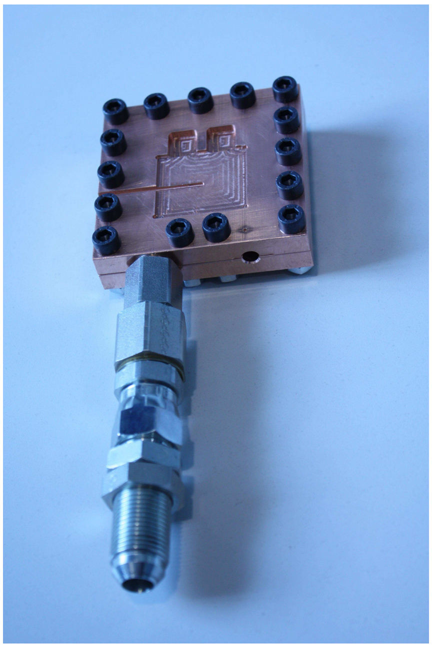

Figure 4.3: Image of the copper coil.

- The space for the tabs of the cells must be sufficiently larger and deep for not having problems of interference with the coil.
- When the liquid nitrogen passes in the coil, for the low temperature the air condenses on the cell (see Figure 4.4), so it is necessary to make the test in a small box in which it is putted gaseous nitrogen.

4.2 Electronic board

To generate the I-V curve for a solar cell it is sufficient to create a small circuit with a series of resistances. Changing the number of resistances it is possible to measure different values of voltage and current to recreate the I-V curve. The problem of this method is that it is very long if are necessary a lot of point and is not much precise. For take the values in few seconds it has been built an electronic board with resistances, capacitors and other components, that is able to recreate the curve and send all the data directly to the computer.

The measuring method utilized is to load the photovoltaic generator by a capacitor and to charge it fully from short circuit to open circuit, and to record the respective voltage and current on function of time. Then with these values the I-V curve can be plotted.

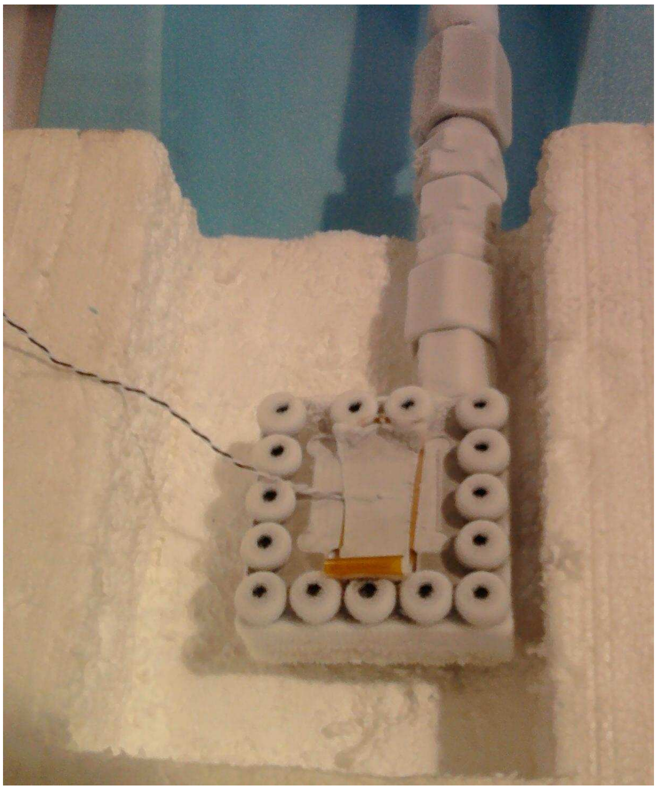

Figure 4.4: Test on the aluminium coil at low temperature with liquid nitrogen.

4.2.1 Deriving the equations of a charging capacitor by PV generator

The equivalent circuit of a poly- or mono-crystalline PV cell, PV module or PV array (PV generator) with its output terminals (a, b) and the capacitor (C) as a load and a shorting switch (s), is presented in Figure 4.5.

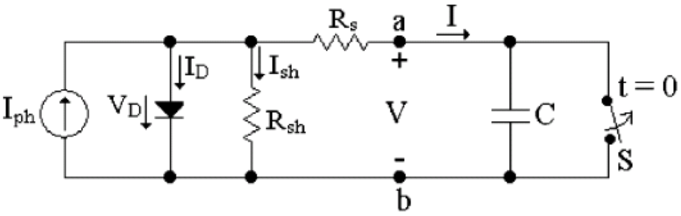

Figure 4.5: Equivalent circuit of a PV cell, module or array (PV generator) with a capacitor as load.

Considering that $R_{sh} \gg R_s$ which means that $I_{sh} \ll I$ [34], and applying the Kirchoffs current and voltage laws to the above circuit, we obtain the following equations:

$$I_D + I = I_{ph} \tag{4.1}$$

$$R_S I + V = V_D \tag{4.2}$$

where I_{ph} is the generated photocurrent (that is constant in time, because the illumination is constant), I_D is the diode current, I is the load current (or the capacitor charging current), V_D is the diode voltage, R_S is the series resistance and V is the voltage at the load. Differentiating Eqs. 4.1 and 4.2 with respect to time, we obtain the following first-order differential equations:

$$\frac{dI_D}{dt} + \frac{dI}{dt} = \frac{dI_{ph}}{dt} = 0 \tag{4.3}$$

$$R_s \frac{dI}{dt} + \frac{dV}{dt} = \frac{dV_D}{dt} \tag{4.4}$$

The characteristic equation of the diode is given by [35]

$$I_D = I_0 \left[\exp\left(\frac{V_D}{AV_T} \right) - 1 \right] \tag{4.5}$$

$$V_D = V_T \ln \left(\frac{I_D + I_0}{I_0} \right) \tag{4.6}$$

where V_T is thermal voltage, A is the ideality factor (A≈1) and I_0 is the reverse saturation current of diode (for Si diode $I_0 = 10^6$ A/cm^2). In addition, it applies for the capacitor:

$$\frac{dV}{dt} = \frac{I}{C} \tag{4.7}$$

$$V_D = V_T ln \left(\frac{I_{ph} - I + I_0}{I_0} \right) \tag{4.8}$$

$$\frac{dV_D}{dt} = -V_T \left(\frac{1}{I_{ph} - I + I_0} \right) \frac{dI}{dt} \tag{4.9}$$

Substituting 4.7 and 4.9 in Eq. 4.4 we obtain the first-order differential equation

$$\left[R_S + \frac{V_T}{(I_{ph} - I + I_0)} \right] \frac{dI}{dt} + \frac{I}{C} = 0 \tag{4.10}$$

In order to obtain the highest speed of change for I(t) and V(t) we should set $R_S = 0$ and then integrate Eq. 4.10 [36]:

$$\int \frac{CV_T}{I(I_{ph} - I + I_0)} dI + \int dt = A$$
$$\frac{CV_T}{I_{ph} + I_0} \ln I - \frac{CV_T}{I_{ph} + I_0} \ln(I_{ph} + I_0 - I) + t = A$$

The integration constant A is obtainable from the initial conditions

$$I(t = 0) = I_{ph}$$
$$I(t) = \frac{I_{ph} + I_0}{1 + \frac{I_0}{I_{ph}} \exp\left(t \frac{I_{ph}+I_0}{CV_T}\right)} \tag{4.11}$$

With $R_S = 0$ and Eqs. 4.1, 4.2, 4.5, and 4.11 we obtain V(t):

$$V(t) = V_T \ln\left[\left(\frac{I_{ph} + I_0}{I_0}\right)\left(1 - \frac{I_{ph}}{I_{ph} + I_0 \exp\left(t \frac{I_{ph}+I_0}{CV_T}\right)}\right)\right] \tag{4.12}$$

The pen-speeds in the Y and X directions of the X–Y recorder are proportional to dI/dt and dV/dt, respectively,:

$$\frac{dI}{dt} = -\frac{I_0 I_{ph}(I_{ph} + I_0)^2}{CV_T} \frac{\exp\left(t \frac{I_{ph}+I_0}{CV_T}\right)}{\left[I_{ph} + I_0 \exp\left(t \frac{I_{ph}+I_0}{CV_T}\right)\right]^2} \tag{4.13}$$

Considering the capacitor Eq. 4.7 with Eq. 4.11 we obtain dV/dt:

$$\frac{dV}{dt} = \frac{I_{ph}}{C} \frac{I_{ph} + I_0}{I_{ph} + I_0 \exp\left(t \frac{I_{ph}+I_0}{CV_T}\right)} \tag{4.14}$$

The maximum pen-speed in I-direction at the X–Y recorder is given at time t_M. The time t_M is determined by the following equations:

$$\left.\frac{d^2 I(t)}{dt^2}\right|_{(t=t_M)} = 0 \tag{4.15}$$
$$t_M = \frac{CV_T}{I_{ph} + I_0} \ln \frac{I_{ph}}{I_0} \tag{4.16}$$

Substituting Eq. 4.16 in 4.11 then in 4.13 we obtain:

$$I(t_M) = \frac{I_{ph} + I_0}{2} \tag{4.17}$$
$$\left.\frac{dI}{dt}\right|_{(t=t_M)} = -\frac{(I_{ph} + I_0)^2}{4CV_T} \tag{4.18}$$

The maximum pen-speed in V-direction at the X–Y recorder is given at time t = 0. Substituting this value in Eqs. 4.12 and 4.14.

$$V(0) = 0 \tag{4.19}$$

$$\left.\frac{dV}{dt}\right|_{t=0} = \frac{I_{ph}}{C} \tag{4.20}$$

At t=0, V(0)=0 and the short circuit current (Isc) of the PV generator flows in the capacitor; setting t=0 in Eq. 4.11 we obtain

$$I(0) = I_{ph} \approx I_{sc} \tag{4.21}$$

At t=∞ the capacitor C will be fully charged. Substituting t=∞ in Eq. 4.12, we obtain the open circuit voltage (V_{oc}) of the PV generator:

$$V_{oc} = V_T \ln \frac{I_{ph} + I_0}{I_0} \tag{4.22}$$

Since $I_{ph} \gg I_0$ and $I_{ph} \approx I_{sc}$, Eq. 4.22 will be

$$V_T = \frac{V_{oc}}{\ln \frac{I_{sc}}{I_0}} \tag{4.23}$$

Setting this value in Eq. 4.16, with $I_{ph} = I_{sc}$ in Eq. 4.17, 4.18 and 4.20 we obtain:

$$t_M = C\frac{V_{oc}}{I_{sc}} \tag{4.24}$$

$$I(t_M) = \frac{I_{sc}}{2} \tag{4.25}$$

$$\left|\frac{dI}{dt}\right|_{(t=t_M)} = -\frac{I_{sc}^2}{4CV_T} \tag{4.26}$$

$$\left.\frac{dV}{dt}\right|_{t=0,V(0)=0} = \frac{I_{sc}}{C} \tag{4.27}$$

The charging process of the capacitor is assumed to last t_S (settling time) when $I(t) \approx I_0$ and, with Eq. 4.23, we obtain t_S:

$$t_S = 2C\frac{V_{oc}}{I_{sc}} \tag{4.28}$$

or

$$C = \frac{t_s}{2}\frac{I_{sc}}{V_{oc}} \tag{4.29}$$

Therefore, the capacitor size is directly and indirectly proportional to the short circuit and open circuit voltage of the PV generator, respectively. Furthermore, the higher the speed of the measuring system, the smaller will be the size of the required capacitor [38].

4.2.2 Description of the board

In the Figures 4.6 and 4.7 are reported the pictures of the electronic board and in Table 4.1 all components utilized.

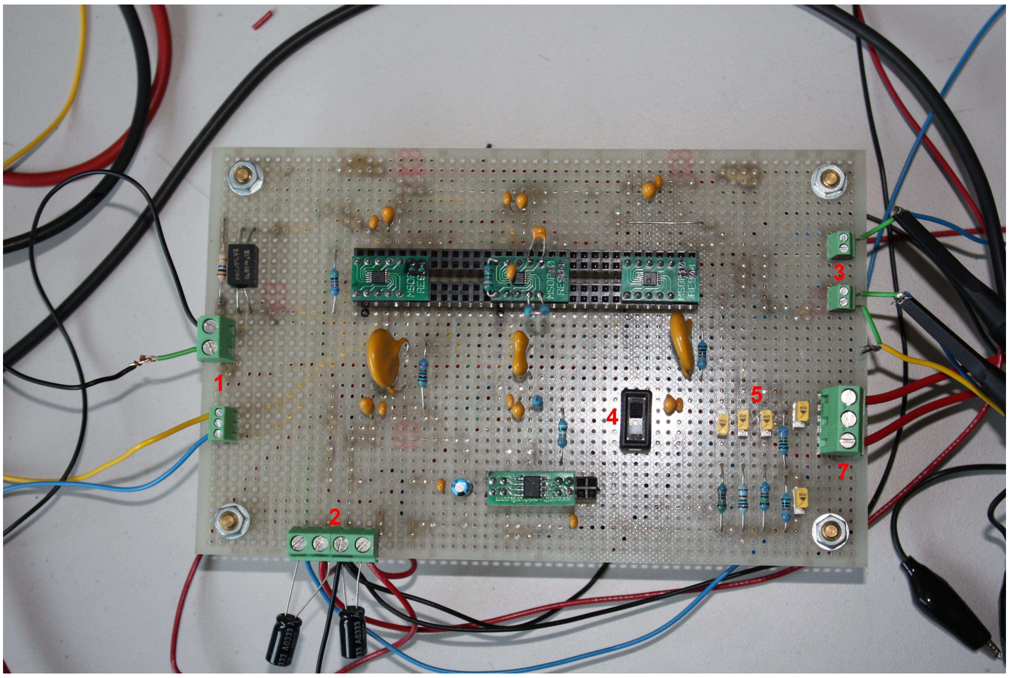

Figure 4.6: Pictures of the first part of the electronic board.

In the following subsection are reported the layout of the principal components that permit to the electronic board to work, all the description refer to the pictures mentioned above.

The solar cell is attached at the terminals numbered with 1 (there are two entrance for "+" and two for "-"), the positive pole is under the cell and the negative are the two small tongues situated on the top of the cell, in the board the positive is signed with a "+".

The board is fed with two different voltages attached at the component numbered with 2 (the components with numbers from 1 to 5 and 7 are in the Figure 4.6, numbers from 6 to 9 are in Figure 4.7), a voltage of 5.07 is attached at "+" mark and a voltage of -0.44 is connected to the "-" sign, all the ground cable going into "m" mark (not visible in the figure).

At the terminal 3 are attached the cable that measured the voltage and the current of the cell, and send all the measures to a matlab file trough the 1208FS-USB device.

It's important to note that there are different switches in the board. The switch with the number 4 positioned in the part with one point "•" indicates

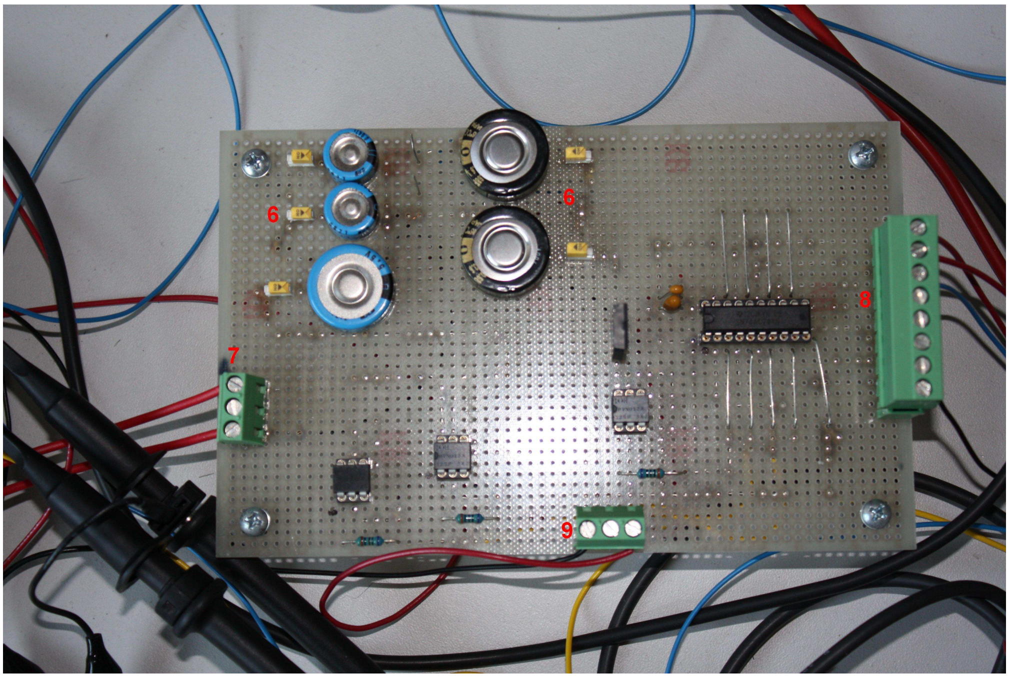

Figure 4.7: Pictures of the second part of the electronic board.

that only one amplifier for the current is in function, in the case that the switch is on two points "●●" indicates that one more amplifier is in function. When the position of this switch is changed the power that feeds the electronic board must be turned off.

The switches at point 5 are to decide what resistance to insert for the gain of the second amplifier, portrayed below. The switches at point 6 in the second board are to decide what capacitor to use, it is possible to use more than one.

The two boards are connected trough a bridge cable signed with number 7 for all two boards and trough a bridge cable for the power supply of 5.07, from the terminal at point 2 in first board to the terminal at point 9 in the second board.

In the terminal numbered with 8 arrives the cable from the 1208FS-USB devices that commands the relays of the board.

In Figure 4.8 it is reported the sketch of function of the electronic board. At the begin there is the photovoltaic solar cell, that is attached with the red cable at the positive and black cable at the negative. In parallel there is attached an operational amplifier that amplify the values of voltage of theoretical 5 times. At a later stage there are two operational amplifier (Figure 4.9) positioned in series at the extremity of a resistance. This element is

Table 4.1: List of components used for the electronic board.

Component	Quantities	Specifications
Amplifier	3	AD 8853
Resistance	2	100 $K\Omega$
	3	301 Ω
	1	40.2 $K\Omega$
	1	3.92 $K\Omega$
	1	475 $K\Omega$
	1	909 $K\Omega$
	1	18.2 $K\Omega$
	1	16.5 $K\Omega$
	1	14 $K\Omega$
Capacitor	1	1 F
	2	0.68 F
	2	0.047 F
	3	0.1 μF
	2	1200 pF
	1	79.3 pF
	1	10 μF
Ceramic disc Capacitor	2	1.2 nF
Radial silveredmica Capacitor	3	100 pF
	1	1000 pF
	1	82 pF
Radial tantalum Capacitor	1	1 μF
Non-polar electrolytic SU	1	10 μF
Relay photovoltaic	3	PVN012APbF
Ultra Low Noise, Precision Voltage Reference	1	ISL21090
Logical buffer	1	
Jumper switch	8	

important for changing the current in voltage, after that the first amplifier gives amplification of theoretical 706, the second amplifier can be made in function with the switch positioned on two points ●●; in this case a more amplify is in function, the values can be decided on the basis of the resistance inserted.

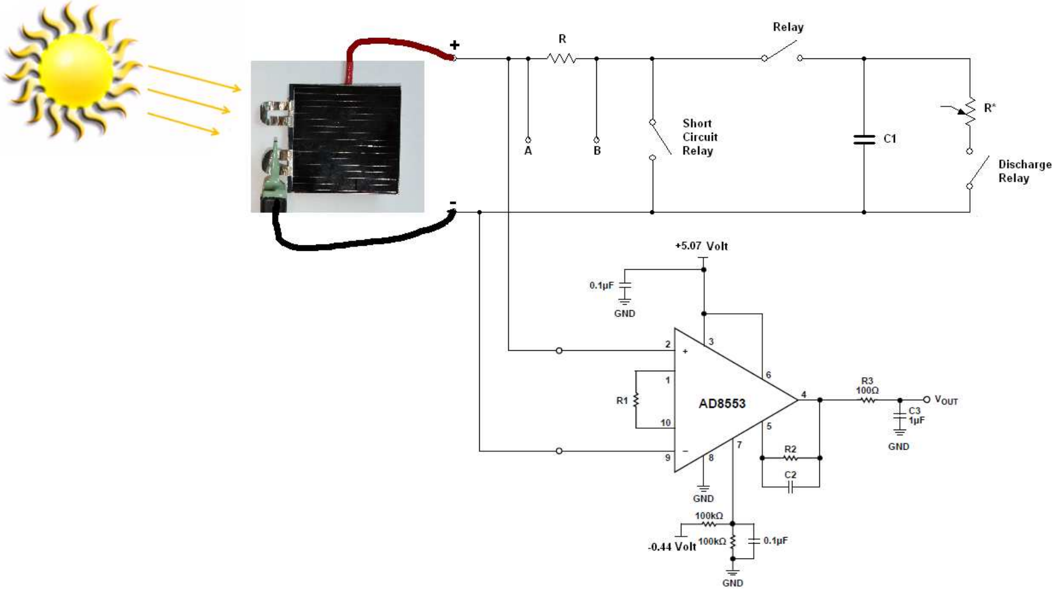

Figure 4.8: Sketch of the scheme of the electronic board.

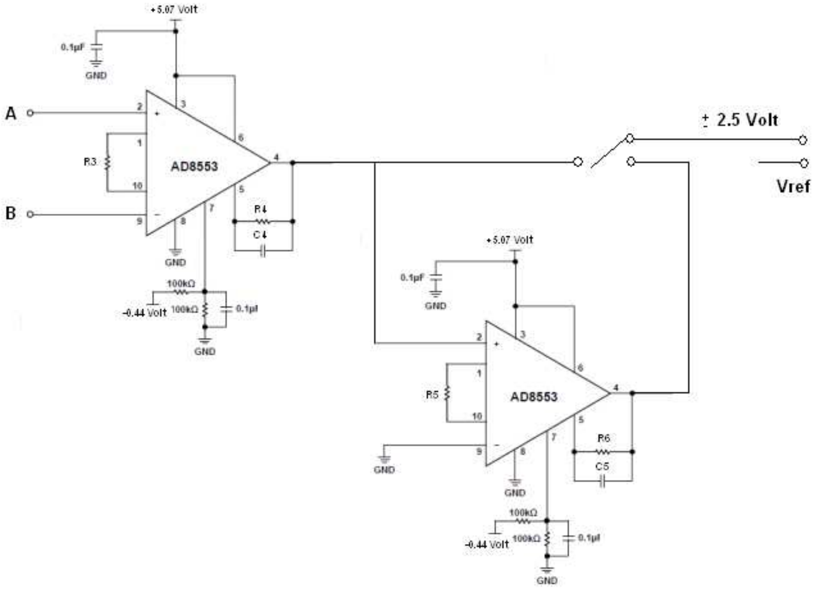

Figure 4.9: Sketch of the two operational amplifier for the current.

The gain of an operational amplify is given by the resistances used:

$$G = 2\frac{R2}{R1}$$

In this case the resistance R2 (in the Figure 4.9 is named R6) is fixed at 100 kΩ, the resistance R1 (in Figure 4.9 is R5) con be inserted trough a switch, in Table 4.2 are reported the values of the resistances with the respective gain of the operational amplifier:

Table 4.2: Resistances that can be inserted in the second amplifier of the current and respective gain of the operational amplifier.

Value of resistance R1 [kΩ]	Gain of the amplifier
200	1
100	2
18.2	10.98
16.5	12.12
14	14.28

After the amplifiers there are two relays in parallel. The "Short Circuit Relay" when is closed cut the rest of the circuit and permits to all the current to pass to this part. The "Relay" when closed permits at the current to go in the capacitor, whereas the "Discharge Relay" permits at the variable resistance to be inserted in the circuit. How this relays work is described in the subsection 4.2.3.

4.2.3 Software for data acquisition

The management of the data acquisition and the commands is done by the USB-1208FS and it is interfaced with the "data acquisition toolbox" of matlab (Simulink). To start the data acquisition it is necessary to run the matlab file "data_acquisition", this permits Simulink to start the simulation for collecting all data. In Simulink there are two blocks that command the USB, one is a digital output that commands the three relay of the circuit: Discharge Relay, Relay and Short Circuit Relay, as shown in Figure 4.8, the second is an analog input block that receives the values of voltage and current.

In the Figure 4.11 it is possible to see the diagram that manage the relays. In principle there is a clock that manages the time, the switches that manage the relays are activated at different time.

At the beginning all the relays are open. At time 1 the system closes the "Discharge Relay", in this way the configuration permits to the capacitor to discharge trough the resistance insert in parallel with the capacitor. At time 2 the "Short Circuit Relay" is closed; at this moment all the current passes

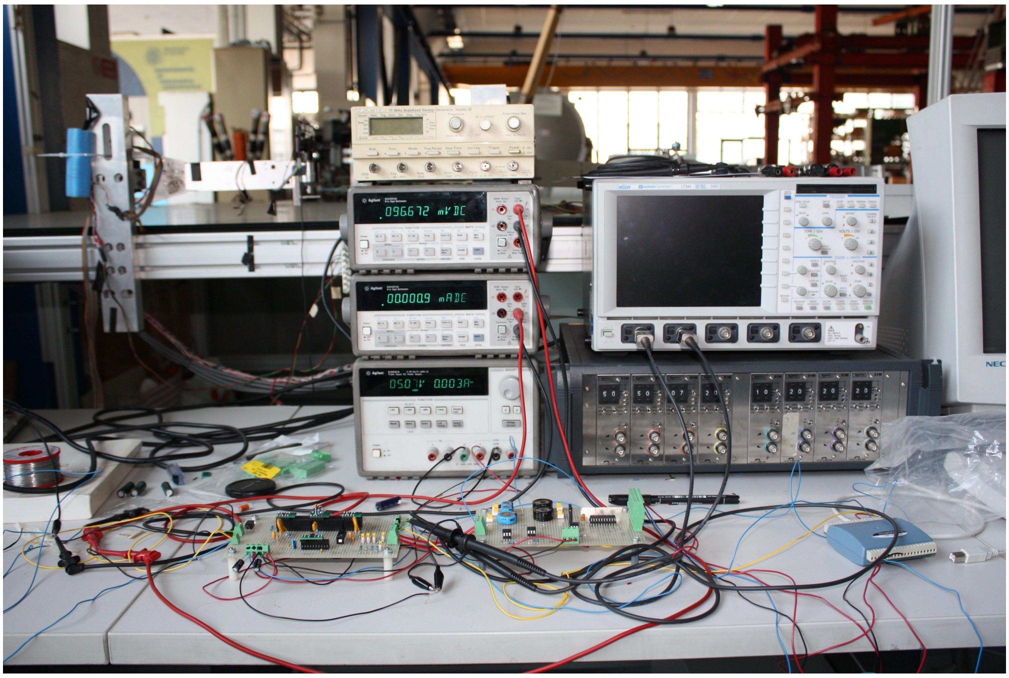

Figure 4.10: Pictures of the experimental apparatus in laboratory for testing the electronic board.

trough this line. At time 3 the last Relay is closed with no consequences on the circuit. At time 4 the “Discharge Relay” would be opened in order to permit to the current to charge the capacitor when at time 5 the “Short Circuit Relay” would be opened. From time 5 to time 10 happens the charge of the capacitor, then the simulation finishes.

For all the simulation the program collects all the data, but to recreate the I-V characteristic it is important to consider only the data when the capacitor begins to charge till the end of the simulation.

4.2.4 Characterization of the operational amplifier

The operational amplifiers were chosen to work at precise values of gain, unfortunately the value of gain is different from the theory.

Initially, 4 operational amplifiers were taken. These were soldered at the base with a soldering iron tip at 300°C, these are named: A, B, C and D. Later, cause the values were strange, other four operational amplifiers were taken, three of them were soldered with hot-air welding and pasta at 300°C, because it was thought that the type of welding could be a cause of the problems, them were named: E, F and G. The last amplifier, named H, was soldered as the first four.

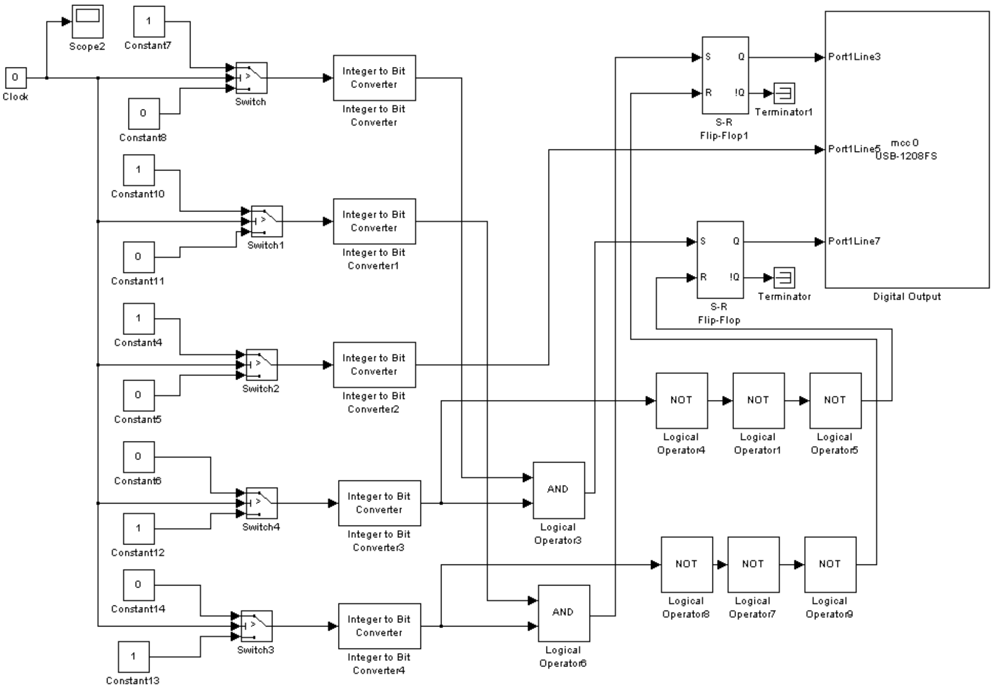

Figure 4.11: Blocks in Simulink file for the management of the relays of the electronic board.

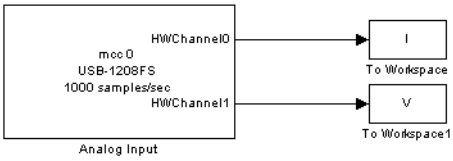

Figure 4.12: Blocks in Simulink file for the acquisition of the values of voltage and current.

To verify the effective gain, a test was made for the voltage and one for the current.
As said in subsection 4.2.2 the gain for an amplifier is given by the relation between the resistances, that is:

$$G = 2\frac{R2}{R1}$$

For the voltage R2 is 100 kΩ and R1 40.2 kΩ that make a gain of 4.975, whereas for the first amplifier of the current R2 is 1384 kΩ and R1 is 3.92

kΩ, so the gain is 706.12.
For the voltage were tested all the amplifiers to verify if all them work in the same mode.
For this verification it was taken a generator of voltage and used in place of the cell, then the circuit was powered with a voltage of 5.07 and -0.44 to permit at the operational amplifier to work. The value of the generator was changed from zero to 1 Volt with small intervals, and these were the V_{in}. With a multimeter the values of voltage after the operational amplifier were registered, named V_{out}, these values are in the range of -2.5 and +2.5, that is the range of working of the schedule, for calculation the gain this values are adjusted with the addition of +2.5.
To calculate the gain for the voltage the following formula was utilized:

$$G = \frac{(V_{out} + 2.5) - V_{ref}}{V_{in}}$$

where V_{ref} is a value of voltage, that can be addicted in the operational amplifier, for have the exit voltage in a range required.
Following are reported the values for the calculation of the gain for the amplifier A (Table 4.3) and E (Table 4.4).
With this result it is possible to note that the values of gain are around the value of 5 expected, only the firsts numbers are slightly lower.
For the fact that all the operational amplifiers worked in similar mode, it was decided that, for characterization the gain for the current, is necessary to use only two amplifiers: one when is used only one amplification and two when there is an other amplification, but to compare the results in the second case the gain of the second amplifier is one.
Initially the circuit was made in short circuit condition, in this mode the current is at his maximum, so at I_{sc}, and the voltage is null. In this condition is possible to calculate the gain with the following formula:

$$G = \frac{I_{out}}{I_{in}}$$

where I_{in} is the current generated from a generator of current from 0 to 7 A and changed in Volts with a resistance, I_{out} is the voltage after the gain.
Observing this result, Table 4.6 with only one amplifier and Table 4.5 with two, it is immediately evident that for values of current under 200 mA the gain is not constant and significantly under the theoretical value. From 200 mA to 700 mA the gain remain around 700, that is little less than 706 theoretical. In the second case the values of gain are a little less than in the first, but remain the strange trend of the curve. To mark this problem the results are inserted in a graph (see Figure 4.13), in that is possible to read

Table 4.3: Calculation of the gain for the voltage with the operational amplifier "A", the theoretical gain is 5.

V_{out} [V]	V_{out}+2.5 [V]	V_{in} [V]	V_{ref} [V]	G	error %
-2.482	0.018	0.004	0	4.286	
-2.233	0.267	0.054	0	4.944	-13.323
-1.984	0.516	0.104	0	4.971	-0.536
-1.732	0.768	0.154	0	4.987	-0.319
-1.481	1.019	0.204	0	4.995	-0.162
-1.230	1.270	0.254	0	5.000	-0.098
-0.981	1.519	0.303	0	5.013	-0.263
-0.731	1.769	0.354	0	4.997	0.321
-0.481	2.019	0.404	0	4.998	-0.007
-0.230	2.270	0.454	0	5.000	-0.050
0.018	2.518	0.504	0	4.996	0.079
0.283	2.783	0.554	0	5.023	-0.546
0.541	3.041	0.604	0	5.035	-0.224
0.809	3.309	0.654	0	5.060	-0.491
1.065	3.565	0.704	0	5.064	-0.085
1.341	3.841	0.754	0	5.094	-0.594
1.597	4.097	0.804	0	5.096	-0.032
1.832	4.332	0.854	0	5.073	0.457
2.056	4.556	0.904	0	5.040	0.650
2.270	4.770	0.954	0	5.000	0.796
2.425	4.925	0.994	0	4.955	0.914
2.452	4.952	1.000	0	4.952	0.055

the gain in function of the current for both cases.

To understand this problem the technical support of the Analog Device was contacted, from this exchange of emails was identify some possible causes of this problem were identified:

- The operational amplifier is very small, for this reason the resistances and capacitors used must be very small (in dimension).
- The components attached symmetrical must have symmetrical length of cables.
- The components must be soldered near the operational amplifier, the presence of cable can be given losses and interferences.

Table 4.4: Calculation of the gain for the voltage with the operational amplifier "E", the theoretical gain is 5.

V_{out} [V]	V_{out}+2.5 [V]	V_{in} [V]	V_{ref} [V]	G	error %
-2.482	0.018	0.004	0	4.286	
-2.234	0.266	0.054	0	4.926	-12.997
-1.984	0.516	0.104	0	4.971	-0.909
-1.732	0.768	0.154	0	4.984	-0.267
-1.482	1.018	0.204	0	4.992	-0.145
-1.231	1.270	0.254	0	4.998	-0.127
-0.982	1.518	0.304	0	4.996	0.033
-0.731	1.769	0.354	0	4.997	-0.005
-0.481	2.019	0.404	0	4.997	-0.008
-0.231	2.269	0.454	0	4.997	0.002
0.017	2.517	0.504	0	4.994	0.065
0.266	2.766	0.554	0	4.993	0.017
0.516	3.016	0.604	0	4.993	0.005
0.763	3.263	0.654	0	4.989	0.065
1.011	3.511	0.704	0	4.987	0.042
1.263	3.763	0.754	0	4.991	-0.070
1.522	4.022	0.804	0	5.002	-0.235
1.778	4.278	0.854	0	5.009	-0.137
2.027	4.527	0.904	0	5.008	0.032
2.253	4.753	0.954	0	4.982	0.513
2.424	4.924	0.994	0	4.954	0.574
2.467	4.967	1.000	0	4.967	-0.267

Searching to solve this problem it was taken the first amplifier for the current (in Figure 4.6 is the amplifier in middle), and the principal resistances was soldered directly to the amplifier. Unfortunately, this change did not lead to any improvement.

Table 4.5: Calculation of the gain for the current with two operational amplifier insert, the first with a theoretical gain of 706, the second a theoretical gain of 1.

I_{out} [A]	I_{in} [V]	I_{in} [mA]	G1
0.039	0.099	9.92	393.145
0.140	0.243	24.3	574.074
0.217	0.353	35.3	614.731
0.325	0.504	50.44	643.537
0.388	0.594	59.35	652.991
0.457	0.693	69.26	659.833
0.530	0.797	79.7	664.994
0.608	0.907	90.68	670.159
0.695	1.030	102.96	675.019
0.700	1.036	103.6	675.676
0.755	1.118	111.8	675.313
0.989	1.457	145.7	678.449
1.411	2.045	204.5	689.976
1.688	2.442	244.2	691.237
1.925	2.774	277.4	693.944
2.115	3.044	304.4	694.809
2.418	3.472	347.2	696.429
2.715	3.891	389.1	697.764
2.835	4.064	406.37	697.640
3.052	4.364	436.44	699.294
3.645	5.204	520.4	700.423
4.315	6.162	616.2	700.260
4.716	6.730	673	700.743
5.053	7.266	726.6	695.445

Table 4.6: Calculation of the gain for the current with only one operational amplifier insert, with a theoretical gain of 706.

I_{out} [A]	I_{in} [V]	I_{in} [mA]	G2
0.041	0.095	9.5	431.579
0.121	0.208	20.8	581.731
0.188	0.303	30.3	620.462
0.333	0.508	50.8	655.512
0.393	0.593	59.3	662.226
0.454	0.681	68.13	665.639
0.535	0.795	79.48	672.496
0.615	0.907	90.7	677.619
0.699	1.027	102.7	681.013
0.687	1.009	100.87	681.075
0.757	1.109	110.9	682.597
0.956	1.390	139	687.770
1.403	2.020	202	694.554
1.719	2.470	247	695.951
1.925	2.763	276.3	696.706
2.151	3.083	308.3	697.697
2.367	3.390	339	698.230
2.666	3.815	381.5	698.820
2.848	4.070	407	699.754
3.066	4.380	438	700.000
3.667	5.232	523.2	700.879
4.315	6.155	615.45	701.113
4.693	6.687	668.7	701.809
4.923	7.013	701.3	701.982

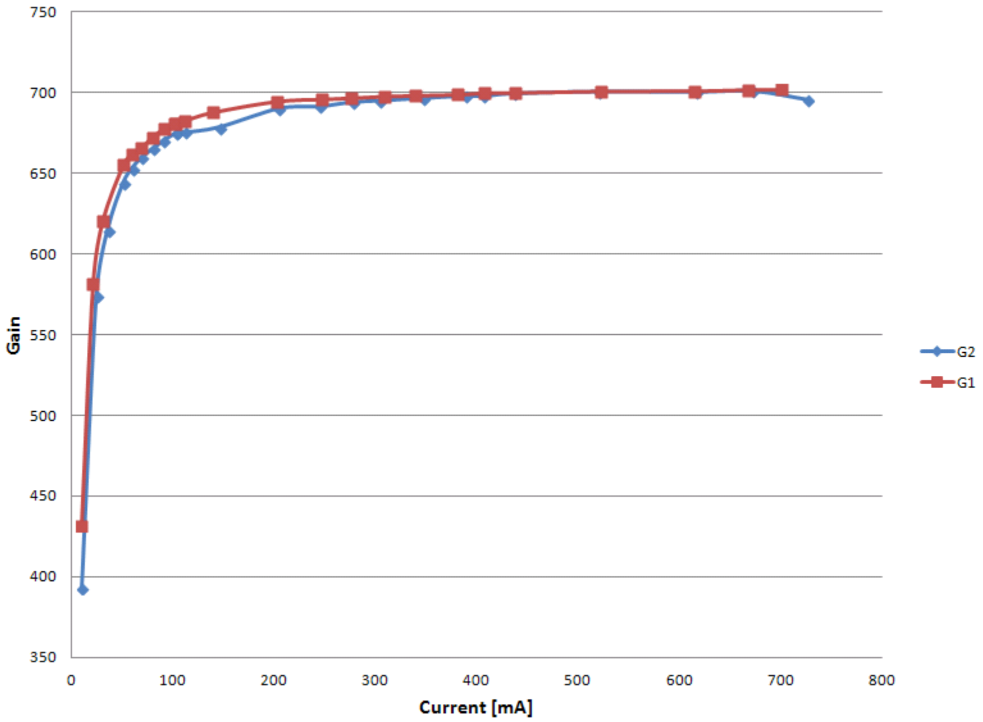

Figure 4.13: Graph of the current in mA and respective gain, G1 is with only one operational amplifier, G2 with two operational amplifier, in both cases the theoretical gain must be 706.

Chapter 5

Tests

5.1 State of test

5.1.1 Tests carried out

The solar cells on the Philae lander were submitted to different tests of characterization, experimental and numerical, which were mainly carried out by the Politecnico di Milano, the Officine Galileo (now selex Galileo) and the ESTEC (European Space Research and Technology Centre). The results obtained by the Officine Galileo and by the ESTEC are described in the Alenia report. All the tests were carried out at BOL. Indeed, the data for the EOL were obtained using the test carried out on Rosetta orbiter solar cells at EOL by INTA (Instituto Nacional de Tecnica Aeroespacial).

5.1.2 Alenia report

In the Alenia reports are the results of the tests carried out during the manufacturing of 6 panels. The tests were carried out by Officine Galileo and ESTEC, the first, however, has only used single flash, while the second single and multiple flash. In both cases, the tests were done in a laboratory environment, at a temperature of +25°C and at the solar constant of 1 and 0.11. The tests of Galileo have been made in different phases: after manufacturing and after thermal vacuum chamber; while those of ESTEC have been made before and after acoustic noise.
These tests show that the Philae solar array complies all requirements at each tested condition. The panel Wall 2 is an exception since it seems to have degradations in the V_{max} and I_{max} in the first test on the acoustic noise however the P_{max} remains constant. These tests are given in the document entitled Alenia SD0646 “Hood solar panels test” [24].

The document SD0621 ”Rosetta Lander Solar Array Design Report” [25] describes the tests performed by Officine Galileo on 6 panels at 0.11 SC, +20°C and -80°C. It also compares results from Officine Galileo with those provided by INTA.

Another remarkable document is the SP00000852 “Solar array simulator support software” [26], which results from Galileo’s studies. This document is the manual for the software that simulates the behaviour of the panels. The simulator has the following input: the radiation dose from 0 to 6.4 in $10 \times 10^{14}\,\mathrm{e\,cm^{-2}}$, the temperature from -150 to +50 °C, the solar constant from 0 to 1, the direction angle of latitude alpha from -180° to +180°, the angle beta (which defines the direction of longitude) from 0° to 90°, and the number of damaged strings for each section from 0 to 2. Is important to note that the software has a good accuracy for values at BOL at environmental temperature (error less than 1%), but so far it has not been validated with data from a space mission.

5.1.3 Test made by Politecnico di Milano

The tests were carried out by Stefano Brambillasca in 2009 as part of his thesis “Celle solari per missioni verso corpi celesti lontani dal sole” [1]; they were performed in LILT condition at CESI (Centro Elettrotecnico Sperimentale Italiano).

Such tests were made on 10 cells approved by the Max Planck Institut für Sonnensystemforschung as appropriate to the mission (“good for flight”)

They were carried out at BOL; a first test was done at a temperature of +25°C at 1 and 0.1 SC, then tests were performed at 0.1 SC and by varying the temperature from +25°C to -120°C with intervals of 10°C between 0 and 100 and intervals of 5°C between 100 and 120.

5.1.4 Test made by INTA

Most of tests made by INTA have been carried out on the Rosetta orbiter cells which indeed are larger than the cells of the lander: $23{,}39\,\mathrm{cm}^2$ versus $10{,}92\,\mathrm{cm}^2$ of Philae. The performed tests are shown in Table 5.1.

Using data from the cells of the orbiter at EOL were obtained, by applying certain formulas, data at EOL for the cells of the lander.

5.1.5 Tests to be made

In the document “Remaining questions regarding Rosetta Philae solar generator” [31] Dr. J. Biele from DLR mentions some tests that could done by

Table 5.1: Characteristics of the tests made on the orbiter and on the lander of Rosetta at INTA

Orbiter (cells area 23,39 cm^2**)**		
SC	**Temp(°C)**	**Fluence** (10×10^{14} e cm^{-2})
1	from +25 to +150	from 0 to 9
0.03	from -155 to +25	from 0 to 9
0.11	+25	0
0.11	from -130 to +25	3.2 and 6.4
Lander (cell area 10,92 cm^2**)**		
SC	**Temp(°C)**	**Fluence** (1×10^{14} e cm^{-2})
0.11	+25	0

PoliMi in the future; he suggests to remeasure cells at BOL, and after irradiation of the cells measure the values at EOL (but with a wire mesh filter to recheck the TC at BOL) , to record the IV curve in detail (512 points) and to measure the IV curve at low intensity 0.0121 SC with 2 filters 0.11.
Other tests to be performed are those envisaging the partial coverage (shadowing) of cells and panels to analyse their respective behaviour at EOL. These tests are crucial since during the landing on the comet there is a risk of dust or ice deposition on the panels.

5.2 Dark current characterisation

As mentioned in the Chapter 2, the relationship between the current and the voltage of a solar cell can be illustraed on a graph. Figure 5.1 shows that the position of the curve depends on the intensity of illumination; if there is no illumination, the cell is in situation of dark current so that the curve in the first quadrant overlaps with the X axis, while the graph in the second quadrant is flat and suddenly grows exponentially, forming the so called “knee”.

5.2.1 Experiment on Philae solar cell

The reverse characterization of the cells is critically important to face the problem of shadowing. In fact, the Philae solar cells can reach the voltage

Table 5.2: Summarizing table of the documents

Document	S.C.	Temp. °C	Fluence	Note
Solar hood panels test report	0.11 and 1	+25	BOL	test on all panels after manufacturing
Solar hood panels test report	0.11 and 1	+25	BOL	test on all panels after thermal vacuum chamber
Solar hood panels test report	0.11 and 1	+25	BOL	test on all panels after acoustic noise
Rosetta Lander solar array design report	0.11	-80 e +20	BOL	test on all panels
Report on LILT MEASUREMENTS of philae solar cells	0.11 and 1	+25	BOL	test on 10 cells
Report on LILT MEASUREMENTS of philae solar cells	0.11	0–120	BOL	test on 10 cells
Solar array unit description Iss draft	0.11 and 1	25	BOL	test on all panels
Solar array simulator support software	0-1	-150-+50	0-6.4 $x10^{14}e/cm^2$	program for simulations

of 7 V (the value of the voltage depends on the current, the temperature and the solar intensity), however, in dark condition a solar cell reaches only $-6/-8$ V. Given that there are eleven cells in a string, some problems may occur when ten of them are illuminated and only one is in shadow, since in this case the resulting voltage is zero.

The Figure 5.2 reports the reverse dark characterisation for philae solar cells as described in the lander user manual [29]; according to the table the absolute breakdown voltage V_B increases with the increase of the temperature,

which indicates breakdown by the avalanche mechanism [22].
The lander user manual gives the following formula for the nearly linear high-current portion ($50 - 200$ mA) of the reverse I-V dark curve:

$$V_{reversedark}(I,t) = -(7.63{+}2.4I){-}(0.00485{+}0.0031I)t{+}(6.4{\cdot}10^{-6}{-}1.0{\cdot}10^{-4}I)t^2$$

where I is in Ampere, V in Volt, t in °C.

5.2.2 Experiment made at Polimi

The experiments reported by LUM were carried out with strings of 1 or 9 cells in a thermal chamber and different temperatures were tested: +60°C,

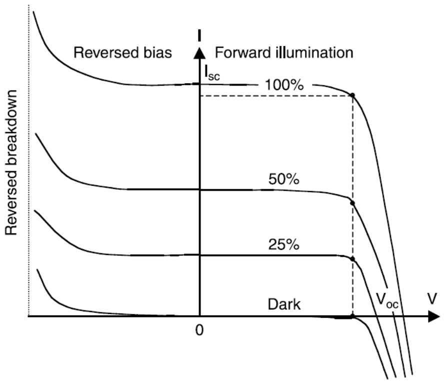

Figure 5.1: Terminal I–V characteristics under full, partial, and zero illuminations.

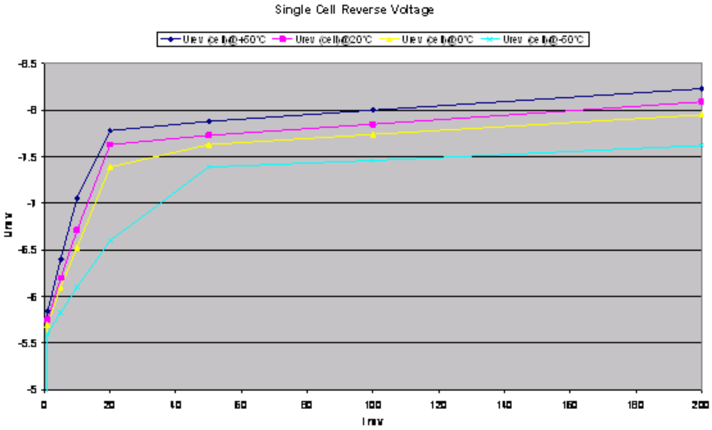

Figure 5.2: Reverse (dark) I-V characteristics for different temperatures present in LUM. I_{rev} in mA, U_{rev} in V [29].

+20°C, 0°C and -60°C. In the graphs showing their results the characteristic curves have been normalized to 1 cell.
The experiments at the Polimi were repeated using only one cell (the number of the cell is L012203) in the thermal vacuum chamber and the temperatures of: +23.2°C, −0.3°C and −20.1°C. For the temperature of 23.2°C the experiments were performed with and without vacuum, for the other temperatures they were made only with vacuum conditions.
The temperature values which were choosen for the experiments are the mean temperature of each point of the curve. For the first point of the curve, when the current is zero, the temperature remains constant; instead, by increasing the cell voltage the intensity of the current also increases thus causing a cell heating; for the last point of the curve, the increase of the temperature is around +14 in the first case and +6.5 in the cold case.
During the experiment the cell in the chamber is connected with a cable to a generator of voltage, starting with a voltage of zero Volt and increasing with intervals of 0.5 Volt until -5 Volt; subsequently the intervals are of 0.2 until reaching -8 Volt; after this value are only considered the points at −8.1 and −8.15 Volt (but not for the cold case).

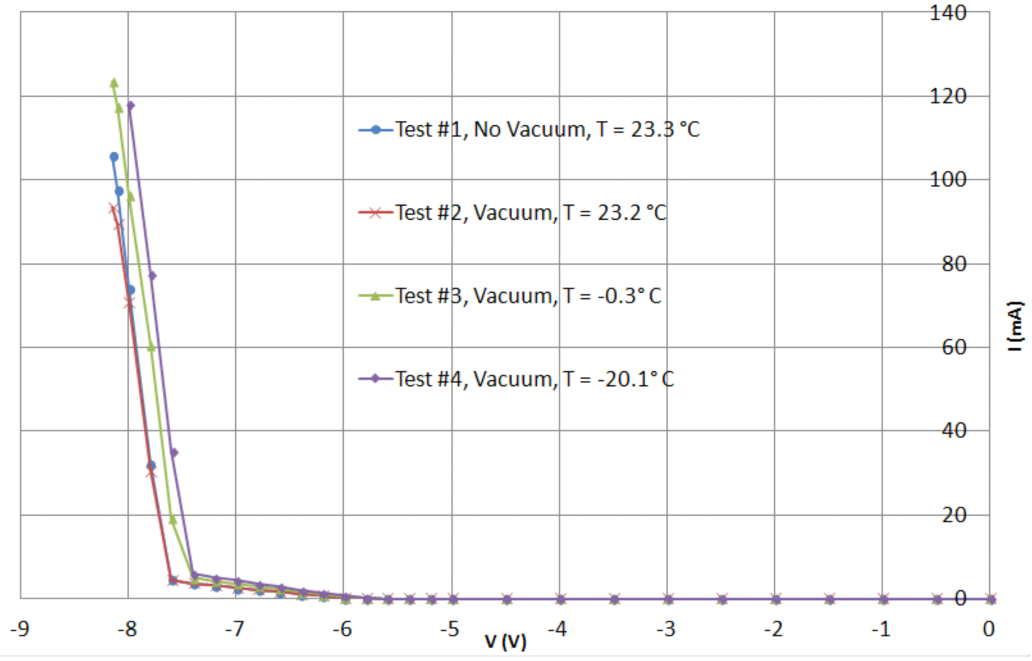

Figure 5.3: Reverse (dark) I-V characteristics for different temperatures in thermal vacuum chamber at the Polimi. I in mA, V in V.

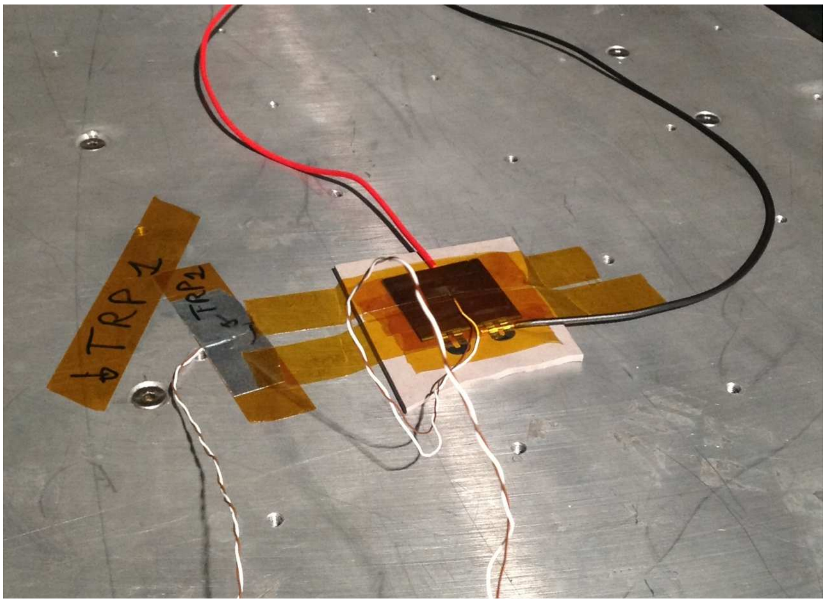

Figure 5.4: The cell in the thermal vacuum chamber.

5.2.3 Consideration

By observing the chart of the results obtained at Polimi (Figure 5.3, it is interesting to observe that the values of the first linear part are the same for all trials, and that for the first trial the values with and without vacuum are approximately the same. When comparing the two experiments, from the Polimi and from the LUM it appears that in both cases the curve becomes progressively narrower with the cooling of the cell; moreover the knee of the curve is situate in the same position, between -7 and -8 Volt.
Taken together, it is possible to conclude that the results obtained at Polimi are consistent with the values presented by the LUM.

5.3 Laboratory conditions test

For testing the validity of the electronic board different tests at different values of solar intensity hare been made. For the illumination of the solar cell it is taken a small incandescent lamp, changing the distance from the cell it is possible to obtain different values of intensity.
Below are reported the results for a test made with the cell number L012203. All the test is monitored with the aid of two multimeters, in this mode is possible to know the I_{sc}, that in this case is 35.1 mA, and the V_{oc}, for this

case is 0.527 V.
At the end of the simulation the program shows four different graph.
The first is the graph of the voltage versus the time (Figure 5.5); it can be seen that at time 5.5 s the electronic board begins to charge the capacitors.

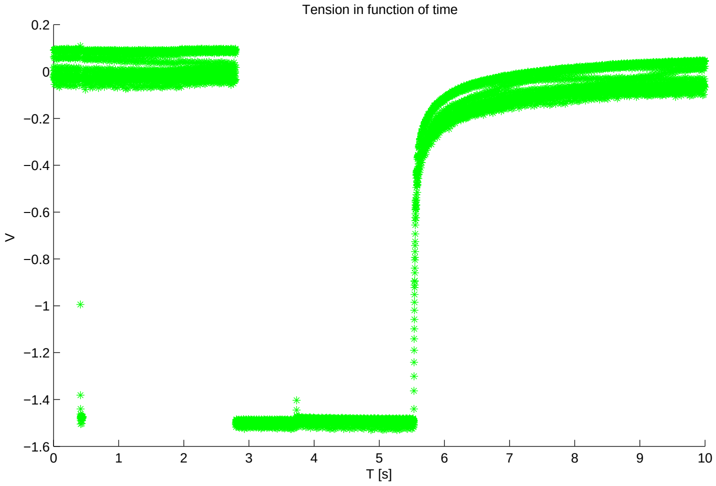

Figure 5.5: Voltage in function of time for the test made on a cell at ambient conditions.

The second is the current in function of time, in Figure 5.6, in this graph it can be seen that many points are out of the trend of the graph, caused by problems of disturbance.
The third graph that the program gives is the I-V curve (Figure 5.7), taken from the values of the former two graphs beginning from the time of 5 s, but in this case the values are in the range of the usb device, that is between the values of -2.5 and $+2.5$.
The last graph, Figure 5.8, is the I-V curve in the real scale; unfortunately the points of beginning of the graph (up left) aren't at the value of zero, but are shifted to right, this is given by problems of resistance inside the cell and in the capacitor, but for the graph is not a big problem because the first part of the I-V curve is linear.
Observing the results is immediately noticed that there are many interferences and there isn't a line but a lot of oscillations, this is caused probably by the lamp, but there were not enough tests to determine the true cause of the problem.

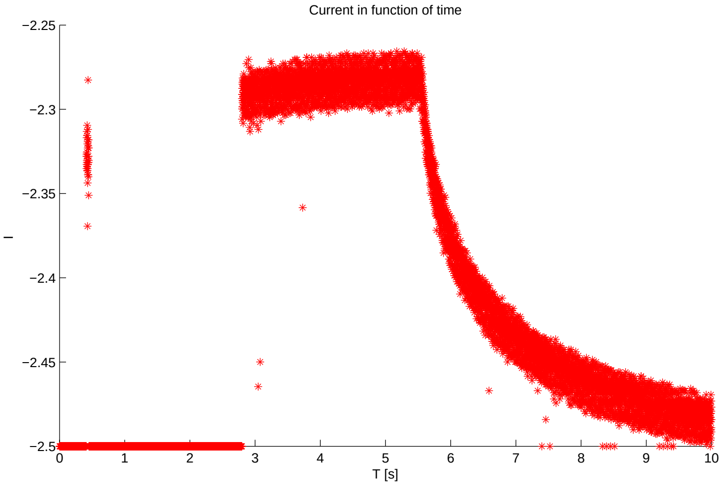

Figure 5.6: Current in function of time for the test made on a cell at ambient conditions.

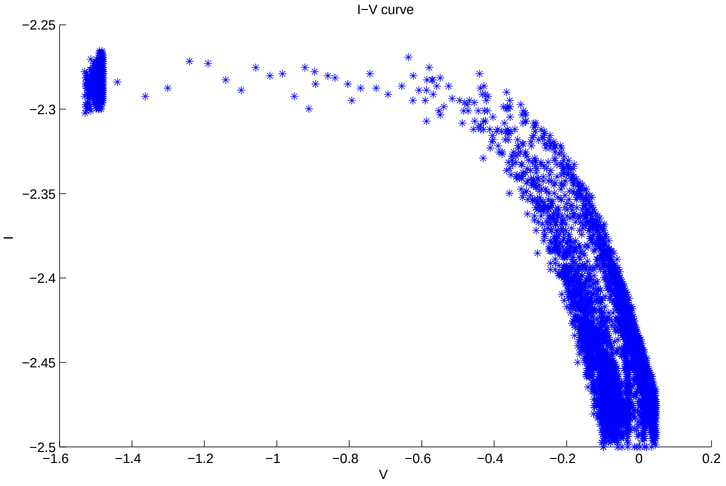

Figure 5.7: Curve I-V for the test made on a cell at ambient conditions in the values of scale of the usb device.

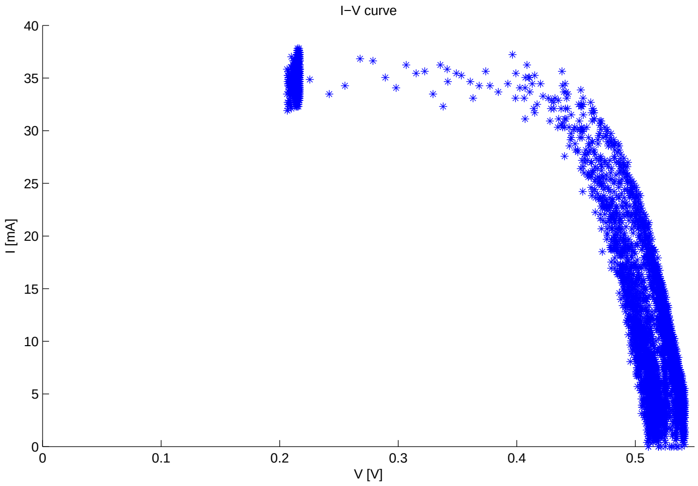

Figure 5.8: Curve I-V for the test made on a cell at ambient conditions.

Chapter 6

Conclusions

The objective pursued for the present work was to create an experimental equipment for characterization of solar cells at low intensity and low temperature. At this scope was realized a cooling coil that permits the cell to reach temperatures under -100°C and an electronic board that takes the values of current and voltage from the cells and sends all the data directly to the computer.

The test made on the cooling coil showed that it doesn't have leakage when it is in function, that reaches low temperature rapidly, and that the cell must be in contact with the coil to have the same temperature measured. Only small devices must be done; the first is to create a slot to permit to insert a cable for the positive pole of the cell, the second is to find a system to adhere well the cell at the coil.

The most problematic work was to create the electronic board. In the board were inserted different resistances and amplifiers for have different gains, but with the test, it results that the operational amplifiers work in strange mode for the different values of current. An other problem found is in the capacitors for the charge: initially were inserted different capacitors with different values that could be inserted or not in the circuit; but the problem of all capacitors used is that all have a big resistance in series, and this doesn't permit to have a lot of point in the I-V curve for the first part, when the capacitors begin to charge. For this reason it is necessary to replace this with capacitors with a smaller resistance in series. Moreover with the equation 4.29 is possible to have an idea of the value of the capacitor. The result from the test showed that there are a lot of interferences in the result, but the graph shows the trend of a normal I-V curve. For this reason it is necessary to make other tests and changes on the board to make it effective to its purpose.

6.1 Future developments

To recreate the final experimental apparatus there is still much work to be done. Below are summarized the key points for the construction of the experimental device and the tests to be performed:

- Design of the base plate and cooling coil: both are made in this thesis.
- Design of the electronic board: it is made in this thesis, but some tests must be done to perform the perfect working of the electronic board, and the capacitors must be changed for have more points in the first part of the curve.
- Box for made the experiments: the box must have an exit for the cables and the pipe for the liquid nitrogen, but is necessary to design an entrance with gaseous nitrogen to not have problems of condensation on the cell. The upper face of the box must be transparent to permit the solar lamp to illuminate the cell, the other walls is better if they are dark for not have problems of interference. An other property to consider in the design is that the cell on the cooling coil must be changed a lot of time.
- Solar lamp: is necessary that this lamp have different filter to make the tests at different values of solar intensity.
- Tests at ambient conditions.
- Tests at LILT conditions at BOL: this test are important to confront new results with the existent results.
- Test at LILT conditions at EOL: it is possible to perform these tests after artificially irradiation of the solar cells.
- Tests whit a partial shadowing.
- Test with the presence of dust.

List of acronyms and abbreviations

67P/CG	67P/Churyumov-Gerasimenko
AM0	Air Mass 0
AR	Antireflection
ASTM	American Society for Testing and Materials
AU	Astronomical Unit
BOL	Begin of life
CESI	Centro Elettrotecnico Sperimentale Italiano
DLR	Deutschen Zentrums für Luft- und Raumfahrt
EOL	End of life
ESA	European Space Agency
FSS	First Science Sequence
HST	Hubble Space Telescope
LILT	Low Intensity Low Temperature
LTS	Long Term Science
LUM	Lander User Manual
MLI	Multi-layer insulation
MPPT	Maximum Power Point Tracker
NASA	National Aeronautics and Space Administration
NTT	New Technology Telescope
Polimi	Politecnico di Milano
RTG	Radioisotopes Thermoelectric Generator
SA	Solar Array
SAS	Solar Array System
SC	Solar Constant
SDL	Separation, Descent, and Landing
WMO	World Meteorological Organization

Bibliography

[1] Stefano Brambillasca, *Celle solari per missioni verso corpi celesti lontani dal Sole*, Tesi di Laurea Politecnico di Milano, 2007/2008.

[2] Giulia Damonte, *Analysis and characterization of Solar cells for mission to Jupiter*, Tesi di Laurea Politecnico di Milano, 2005/2006.

[3] K.-H. Glassmeier, H. Boehnhardt, D. Koschny, et al., *The Rosetta mission: flying towards the origin of the solar system*, Space Science Reviews, Springer, 2007.

[4] KM. Pesco and A. E. Finzi, *Rosetta Space Mission - The Solar Array Photovoltaic Assembly*, at XIX Congresso Nazionale AIDAA, Forlì - Italy, 2007.

[5] Hans S. Rauschenbach, *Solar cell array design handbook, volume 1*, National Aeronautics and Space Administration, Springer, 1976.

[6] European Space Agency, Rosetta mission, *http://sci.esa.int/science-e/www/area/index.cfm?fareaid=13*

[7] Wikipedia, The Free Encyclopedia, *http://www.wikipedia.org*

[8] Amazing Space, *http://http://amazing-space.stsci.edu/*

[9] P. Lamy, I. Toth, et al., *A portrait of the nucleus of comet 67p/Churyumov-Gerasimenko*, Space Science Reviews, Springer, 2007.

[10] Björn J.R. Davidsson, Pedro J. Gutiérrez, *Nucleus properties of Comet 67P/Churyumov–Gerasimenko estimated from non-gravitational force modeling*, Icarus Vol. 176, Elsevier, 2005.

[11] Konrad J. Kossacki , Jacek Leliwa-Kopysty ́nski, Slawomira Szutowicz, *Evolution of depressions on Comet 67P/Churyumov–Gerasimenko: Role of ice metamorphism*, Icarus Vol. 184, Elsevier, 2006.

[12] Masateru Ishiguro, *Cometary Dust Trail Associated with Rosetta Mission Target:67P/Churyumov-Gerasimenko*, Icarus , 2007.

[13] J. Agarwal, M. Muller, G. Eberhard, *Dust environment modelling of comet 67P/Churyumov-Gerasimenko*, Space Science Reviews Vol. 128, Springer, 2006.

[14] R. Schulz, J. A. Stüwe, H. Boehnhardt, *Rosetta target comet 67P/Churyumov-Gerasimenko, Postperihelion gas and dust production rates*, Astronomy & Astrophysics, Eso, 2004.

[15] Flavio Iurato, *Ottimizzazione di celle solari al GaAs per missioni sulla superficie di Marte*, Tesi di Laurea Politecnico di Milano, 2003/2004.

[16] Giulio Pinzan, *Landing Site Selection for Rosetta Lander Philae through a Multidisciplinary Approach*, Tesi di Laurea Politecnico di Milano, 2011/2012.

[17] Gianluca M. Caputo, *On-comet attitude determination of Rosetta lander Philae through nonlinear optimal system identification*, Tesi di Laurea Politecnico di Milano, 2011/2012.

[18] CESI, *Solar cells achievements & road map for space and Earth*, Seminar at Politecnico di Milano, 2012.

[19] C.J. Gerderloos, R.J. Walters, et al., *Low Intensity Low Temperature Performance of Advanced Solar Cells*, IEEE, 2002.

[20] H.Y. Tada, J.R. Carter, et al., *Solar Cell Radiation handbook*, NASA, JPL, 1982.

[21] Harold J. Hovel, *Semiconductors and Semimetals*, Vol. 11: Solar Cells, Academic Press, 1975.

[22] S. M. Sze, *Physics of Semiconductor Devices*, Wiley-Interscience, 1969.

[23] Mukund R. Patel, *Spacecraft power systems*, CRC Press, 2005.

[24] Gwenael Beltrame, Luca Vallini, *Solar hood panels test report*, Alenia, 2001.

[25] Gwenael Beltrame, *Rosetta lander solar array design report*, Alenia, 2001.

[26] M. Barela, *Solar array simulator support software*, Galileo Avionica, 2004.

[27] Gwenael Beltrame, Luca Vallini, *Flight panels test plan and procedure*, Alenia, 2001.

[28] Francesco Topputo, *Report on LILT mesuraments of philae solar cells*, Politecnico di Milano, 2007.

[29] J. Biele, *Solar array unit description Iss draft*, LUM, 2011.

[30] J. Biele and S. Ulamec, *Capabilities of Philae, the Rosetta Lander*, Space Science Review, vol. 138, pp. 275-289, 2008.

[31] J. Biele, *Remaining questions regarding Rosetta PHILAE solar generator*, Comments after telecon with Gianfelice D'Accolti, 27.04.2012.

[32] J. Biele and S. Ulamec, *From the Rosetta lander Philae to an asteroid hopper:lander concepts for small bodies missions*, report and presentation, German Aerospace Center (DLR), 2004.

[33] Imre Toth, *What's new about 67P/CG? - Characterization of the physical properties of the nucleus of comet 67P/CG*, 3^{rd} Post-Launch workshop of the Rosetta Philae Science Team, Konkoly Observatory Budapest, 17 December 2007.

[34] Mahmoud Marwan, Ismail Naban, *Analytical and graphical methods for determination of solar cell parameters and investigations of shadowing effect*, Int J Sol Energy, UK, vol. 9, pp. 179–192, 1990.

[35] L. Nashelsky, R. Boylestad, *Electronic devices and circuit theory*, 6th ed. Englewood Cliffs, NJ: Prentice Hall, 1996.

[36] Mahmoud Marwan, *Investigations on characteristic parameters and power degradation of amorphous silicon solar modules based on long-term outdoor testing*, International Energy Journal, Vol. 2 No. 2, December 2001.

[37] *DLR Rosetta Mission Brochure - Journey to a comet*, Deutsches Zentrum for Luft und Raumfahrt, 2008.

[38] Marwan M. Mahmoud, *Transient analysis of a PV power generator charging a capacitor for measurement of the I–V characteristics*, Renewable Energy, vol. 31 (13) Elsevier, 2006.

[39] VV.AA., *Rosetta Lander - System Status after Five Years in Space*, Aerotecnica Vol.88, No.4, 2009.

[40] F. Topputo, F. Bernelli-Zazzera, F. Ercoli-Finzi, *Solar Array Simulators for Low Power Space Missions*, Proceedings of the 3rd CEAS Air & Space Conference, 2011.